

RELATIVISTIC MERGERS OF SUPERMASSIVE BLACK HOLES AND THEIR ELECTROMAGNETIC SIGNATURES

TANJA BODE¹, ROLAND HAAS¹, TAMARA BOGDANOVIĆ^{2,3}, PABLO LAGUNA¹ AND DEIRDRE SHOEMAKER¹

Draft version November 2, 2018

ABSTRACT

Coincident detections of electromagnetic (EM) and gravitational wave (GW) signatures from coalescence events of supermassive black holes are the next observational grand challenge. Such detections will provide the means to study cosmological evolution and accretion processes associated with these gargantuan compact objects. More generally, the observations will enable testing general relativity in the strong, nonlinear regime and will provide independent cosmological measurements to high precision. Understanding the conditions under which coincidences of EM and GW signatures arise during supermassive black hole mergers is therefore of paramount importance. As an essential step towards this goal, we present results from the first fully general relativistic, hydrodynamical study of the late inspiral and merger of equal-mass, spinning supermassive black hole binaries in a gas cloud. We find that variable EM signatures correlated with GWs can arise in merging systems as a consequence of shocks and accretion combined with the effect of relativistic beaming. The most striking EM variability is observed for systems where spins are aligned with the orbital axis and where orbiting black holes form a stable set of density wakes, but all systems exhibit some characteristic signatures that can be utilized in searches for EM counterparts. In the case of the most massive binaries observable by the Laser Interferometer Space Antenna, calculated luminosities imply that they may be identified by EM searches to $z \approx 1$, while lower mass systems and binaries immersed in low density ambient gas can only be detected in the local universe.

Subject headings: accretion – black hole physics – gravitational waves – hydrodynamics – relativity – shock waves – X-rays: bursts

1. INTRODUCTION

Galactic mergers are expected to be the major route for the formation of binary black holes (BBHs), in agreement with predictions of hierarchical models of structure formation (Haehnelt and Kauffmann 2002; Volonteri, Haardt, and Madau 2003a) and with observations showing that the majority of galaxies harbor supermassive black holes (SMBHs) in their centers (e.g., Kormendy and Richstone 1995; Richstone et al. 1998; Peterson and Wandel 2000; Ferrarese and Ford 2005). Some fraction of newly formed galaxies are thus expected to host binary systems of SMBHs, whose inspiral and merger lie in the “sweet spot” of the future Laser Interferometer Space Antenna (LISA). These cataclysmic cosmic events produce copious amounts of gravitational radiation ($\sim 10^{57}$ erg s⁻¹) during the final stages of merger, radiation which is imprinted with detailed information about the inspiral and merger of the binary as well as the state (mass, spin and kick) of the resulting black hole (BH). Detecting and characterizing these binary mergers will thus be an important resource for understanding formation mechanisms and the cosmological evolution of SMBHs (Volonteri et al. 2003b, 2004; Micic et al. 2007; Sesana et al. 2007). A synergistic detection of electromagnetic (EM) and gravitational wave (GW) radiation from merging SMBHs has been defined as the next observational grand challenge (Kocsis et al. 2006, for example). A combination of EM and GW signatures will provide independent measurements of redshift and luminosity distance, allowing cosmological measurements

at a precision of $\sim 10\%$, limited mainly by uncertainties due to weak gravitational lensing (Hughes and Holz 2003). Similarly, EM+GW observations can be used to test whether gravitons travel at the speed of light, as required by general relativity, and in such a way test one of the fundamental principles of the theory. Furthermore, these multi-messenger observations will provide new insight on accretion processes associated with SMBH binary systems in the final stages of their evolution.

One of the outstanding astrophysical questions with direct bearing on the feasibility of EM+GW detections is regarding the physical properties of the gaseous environment surrounding a binary before and during coalescence. Observationally, a significant sample of these objects is yet to be attained, and finding them in EM searches is a challenging task (Bogdanović et al. 2009). Consequently, most of the information about these systems has to be drawn from theoretical perspectives. Non-relativistic hydrodynamical simulations have, over the past several years, significantly contributed to our understanding of the evolution of BH pairs and interstellar gas, both during and after the galactic mergers (Kazantzidis et al. 2005; Armitage and Natarajan 2002; Escala et al. 2004, 2005; Dotti et al. 2007; Mayer et al. 2007; Colpi et al. 2007; MacFadyen and Milosavljević 2008; Hayasaki et al. 2008; Cuadra et al. 2009). However, simulations spanning the entire dynamical range, from galactic merger scales ($\sim 10^2$ kpc) to binary coalescences ($< 10^{-2}$ pc), are still prohibitively computationally expensive. As a consequence, non-relativistic simulations stop at binary separations of order 1 pc while fully general relativistic simulations are possible only at separations of order 10^{-5} pc. Thus the properties and structure of accretion flows around binaries are uncertain. For instance, the presence of gas on larger scales in the aftermath of a gas rich galactic merger may not guarantee an abundant supply of gas for accretion once

¹ Center for Relativistic Astrophysics, School of Physics, Georgia Institute of Technology, Atlanta, GA 30332, USA

² Department of Astronomy, University of Maryland, College Park, MD 207422, USA

³ Einstein Fellow

a gravitationally bound binary is formed. This is because the binary torques can evacuate most of the surrounding gas, thus preventing any significant accretion on either member of the binary (Milosavljević and Phinney 2005). The scenario in which binary torques clear a central low density region is commonly described in the literature as the *circumbinary disk*. Alternatively, it is also plausible that if the surrounding gas is sufficiently hot and tenuous, the binary may find itself engulfed in a radiatively inefficient, turbulent flow all the way through coalescence. Such conditions could arise in gas deficient mergers and are indeed expected to exist in nuclear regions of some low luminosity active galactic nuclei (AGNs; Quataert 1999; Ptak et al. 2004; Nemmen et al. 2006; Elitzur and Ho 2009, for example). We refer to this scenario as the *gas cloud* and note that if binaries indeed do exist in radiatively inefficient flows, then the *circumbinary disk* and *gas cloud* scenarios effectively bracket the range of physical situations in which pre-coalescence binaries may be found in centers of galaxies.

In addition to EM signatures and accretion, a gaseous environment could potentially have a profound effect on the dynamics of the BHs. For instance, accretion torques in gas rich mergers could force the BHs to have a “preferential” spin orientation, aligning the spins of the BHs with the angular momentum of the large-scale gas disk (Bogdanović et al. 2007). Since numerical relativity (NR) simulations have established that the magnitude of the gravitational recoil on the final BH depends on the spin orientation of the merging BHs (Herrmann et al. 2007a; Koppitz et al. 2007; Campanelli et al. 2007a,b; González et al. 2007; Baker et al. 2007; Schnittman and Buonanno 2007), the presence or absence of gas in the vicinity of the BBH can have direct implications for the magnitude of the kick inflicted on the final BH.

In this work, we build upon the framework of larger-scale simulations as well as the initial relativistic calculations that investigated both the dynamics of test particles (van Meter et al. 2009) and the evolution of EM fields (Palenzuela et al. 2009a,b) in the gravitational potential of a coalescing binary. We use fully general relativistic numerical hydrodynamics simulations to follow the interaction of a BH binary in a gaseous environment through coalescence. We focus on the final stages of the binary evolution (last few orbits and merger) and consider only equal-mass SMBH binaries surrounded by a hot and tenuous gas cloud. The main objective of this work is to characterize the EM and GW signatures that arise during coalescence⁴.

The remainder of this paper is organized as follows: The computational methodology used is described in §2, followed by the initial conditions used in the simulations in §3. We describe the general gas dynamics in §4. In §5, we present a discussion of the EM and GW signatures, followed by our conclusions in §6.

2. COMPUTATIONAL METHODOLOGY

The results in this paper were obtained with the new version of the MAYAKRANC code of the NR group at Georgia Tech. The new code is an enhanced version of the code that was used primarily for studies involving vacuum spacetimes containing BH singularities (Washik et al. 2008; Hinder et al. 2008; Herrmann et al. 2007b,c; Bode et al. 2008; Bode et al.

2009). As with the previous code, the new MAYAKRANC code is based on the BSSN formulation and the moving puncture method (Campanelli et al. 2006a; Baker et al. 2006). The code source is generated by the package KRANC (Husa et al. 2006), which produces a set of *thorns* that work under the CACTUS infrastructure (Allen et al. 1999) and CARPET mesh refinement (Schnetter et al. 2004). The new main feature in the MAYAKRANC code is the inclusion of general relativistic hydrodynamics. The hydrodynamics code in MAYAKRANC is a modified version of the public version of the WHISKY hydrodynamics code developed by the European Union Network on Sources of Gravitational Radiation (Whisky-web; Baiotti et al. 2003). Unless otherwise specified, we use geometrized units where $G = c = 1$ and normalized to the mass of the system M , using the metric signature $(-, +, +, +)$.

MAYAKRANC assumes a perfect fluid with energy momentum tensor

$$T^{\mu\nu} = \rho h u^\mu u^\nu + P g^{\mu\nu} \quad (1)$$

with ρ the rest mass density, $h = 1 + \epsilon + P/\rho$ the enthalpy, P the pressure, ϵ the internal energy per unit mass, and u^μ the 4-velocity of the fluid. The 3-velocity of the fluid is given by $v^i = (u^i/u^0 + \beta^i)/\alpha$, with α and β^i the lapse function and shift vector, respectively. The quantities ρ , v^i and ϵ are considered *primitive* variables. The pressure P and the Lorentz factor $W = \alpha u^0$ are viewed as *auxiliary* variables. The pressure P for all the simulations in the present work is calculated from the Γ -law equation of state $P = \rho\epsilon(\Gamma - 1)$ with $\Gamma = 5/3$. The Lorentz factor is obtained from $u^\mu u_\mu = -1$.

WHISKY uses the *Valencia formulation* (Martí et al. 1991; Banyuls et al. 1997; Ibáñez et al. 2001) of numerical hydrodynamics. That is, the evolution equations are cast into a set of conservation equations of the form

$$\partial_0 \vec{F}^0(\vec{w}) + \partial_i \vec{F}^i(\vec{w}) = \vec{S}(\vec{w}), \quad (2)$$

where $\vec{w} = (\rho, v^i, \epsilon)$ is the vector of primitive variables and $\vec{F}^0 = (D, S^i, \tau)$ the corresponding vector of *conservative* variables defined as:

$$D = \sqrt{\gamma} \rho W \quad (3a)$$

$$S^i = \sqrt{\gamma} \rho h W^2 v^i \quad (3b)$$

$$\tau = \sqrt{\gamma} (\rho h W^2 - P) - D \quad (3c)$$

with γ the determinant of the spatial metric. The vectors \vec{F}^i and \vec{S} are the fluxes and source terms, respectively. For details see Banyuls et al. (1997); Ibáñez et al. (2001).

Our code, MAYAKRANC, modifies the WHISKY code in several important ways. In order to improve efficiency as well as simplify the interface between the hydrodynamics and geometry sectors, we implemented a new construction of the stress-energy tensor $T_{\mu\nu}$ and the corresponding sources appearing in the BSSN equations. Furthermore, in the regions within the apparent horizons (AHs), we impose, as suggested by Faber et al. (2007), the dust limit of the hydrodynamics equations when unphysical data appears during the evolution. We also modified the atmosphere treatment used to model vacuum regions. A filter is in place in the atmosphere domains to avoid spurious increases of fluid densities above the atmospheric threshold limit during temporal updates. The overall structure of the WHISKY code has also slightly changed to be able to work seamlessly with the rest of the MAYAKRANC code.

⁴ Animations of the simulations discussed in this paper can be found at http://www.cra.gatech.edu/numrel/papers/BBH_GasCloud.shtml and http://www.cra.gatech.edu/numrel/papers/BBH_Punctures.shtml

For BBH initial data, the MAYAKRANC code uses the PUNCTURES spectral code developed by Ansorg et al.

(2004). We modified this solver to include matter fields. Since the present work focuses on matter fields initially at rest, the modifications to the 2PUNCTURES code involved only the Hamiltonian constraint. The solutions to the momentum constraint remained unchanged; specifically the Bowen-York type solutions continue to be applicable (Bowen and York 1980). As with the vacuum case, we construct initial data for a BBH in a gaseous environment assuming both conformal flatness and a vanishing trace of the extrinsic curvature. The Hamiltonian constraint thus reads

$$\tilde{\nabla}^2 \psi + \frac{1}{8} \psi^{-7} \tilde{A}_{ij} \tilde{A}^{ij} = -2\pi \psi^5 \rho_o = -2\pi \psi^{-3} \tilde{\rho}_o, \quad (4)$$

where $\rho_o = n^\mu n^\nu T_{\mu\nu} = \rho h W^2 - P$ with n^μ the unit normal to the constant time hypersurfaces. In Eq. 4, conformal quantities have tildes, \tilde{A}_{ij} is the traceless part of the extrinsic curvature, and ψ is the conformal factor such that the spatial metric transforms like $\gamma_{ij} = \psi^4 \eta_{ij}$ with η_{ij} the flat metric. The conformal rescaling $\tilde{\rho}_o = \psi^8 \rho_o$ is necessary in order to guarantee the existence of a solution to the constraint equation (York 1979). It is important to emphasize that the freely specifiable matter field is $\tilde{\rho}_o$. We construct $\tilde{\rho}_o$ from $\tilde{\rho}_o = \psi_{vac}^8 \rho_o$ in which ψ_{vac} is the solution to Eq. 4 in the absence of matter. Given $\tilde{\rho}_o$ constructed in this fashion, the solution to the Hamiltonian constraint yields a different ψ , and thus the new ρ_o does not exactly correspond to the primitive matter fields, $\tilde{\rho}_o$, used in setting up the conformal factor.

The MAYAKRANC code also includes infrastructure to analyze the data produced by the simulations. This infrastructure consists of a set of analysis tools or modules to construct gravitational waveforms, estimating BH kicks and spins, and tracking AHs. With the inclusion of hydrodynamics, more modules were needed. Of particular relevance to the present work, we developed tools to monitor conservation of total rest mass in the system, to compute fluxes of matter both through AHs (accretion) and in the form of outflows from the immediate vicinity of the BHs, and to calculate the integrated luminosity of the emitted light.

We tested the implementation of hydrodynamics in MAYAKRANC through a suite of standard tests. One of the important tests includes verifying the conservation of baryonic mass. While baryonic mass should be conserved everywhere in the spacetime, we consider here the conservation within sub-volumes of the computational domain, which also aids us in testing in which sub-volumes conservation may be problematic. That is, integrating (see Banyuls et al. 1997)

$$\partial_t D + \partial_i [D(\alpha v^i - \beta^i)] = 0 \quad (5)$$

over a constant volume \mathcal{V} with boundary $\partial\mathcal{V}$ yields

$$\dot{\mathcal{M}}_{\mathcal{V}} + \int_{\partial\mathcal{V}} D(\alpha v^i - \beta^i) \hat{r}_i dS = 0, \quad (6)$$

with \hat{r}^i the outgoing unit vector to \mathcal{V} and

$$\mathcal{M}_{\mathcal{V}} = \int_{\mathcal{V}} D d^3x. \quad (7)$$

Time integration of Eq. 6 yields

$$\mathcal{M}(t) = \mathcal{M}_{\mathcal{V}}(t) + \mathcal{M}_{\partial\mathcal{V}}(t) = \text{constant}. \quad (8)$$

where

$$\mathcal{M}_{\partial\mathcal{V}}(t) = \int_0^t dt' \int_{S_h} D(\alpha v^i - \beta^i) \hat{r}_i dS_h. \quad (9)$$

On a given step, we compute \mathcal{M} from Eq. 8 to check how well it remains constant.

As a test of the code, we present here the evolution of a Tolman-Oppenheimer-Volkoff (TOV) star (Tolman 1939; Oppenheimer and Volkoff 1939; Misner et al. 1973) of mass $1.4M$, where M is the arbitrary mass scale in the simulation. A TOV star is a static, spherically symmetric solution to the Einstein equations for a spacetime with a perfect fluid. As such, the stability of an evolved TOV is a standard test in numerical relativity with hydrodynamics. The initial data is created by solving the TOV equations, assuming a polytropic equation of state $P = \kappa \rho^\Gamma$ with $\kappa = 100$ and $\Gamma = 5/3$. The computational grid for these test runs consisted of 5 refinement levels extending to an outer boundary of $512M$, the finest of which lay within the star. We evolved this system for three resolutions where we chose the resolutions on the finest refinement level as $M/8$, $M/11.25$, and $M/16$. In the top panel of Fig. 1 we plot the errors in baryonic mass conservation, $\delta\mathcal{M}/\mathcal{M}_0 = (\mathcal{M} - \mathcal{M}_0)/\mathcal{M}_0$, as a function of time with \mathcal{M} computed from Eq. 8 and $\mathcal{M}_0 = \mathcal{M}(t=0)$. In the bottom panel of Fig. 1, we show the corresponding errors in the central density, ρ_{\max} , over $500M$ of evolution time. The central density stays within an acceptable 1.5%. The baryonic mass conservation on the other hand shows a linear increase of errors for the coarsest level of resolution of $M/8$. This error growth arises from the refinement boundaries in the vacuum regions, which are modeled as a low density atmosphere. As each boundary comes into causal contact with the surface of the star, the density rises above atmospheric levels despite our atmospheric filters, adding a mass violation. While this effect is significant in the coarsest run, the errors remain below 0.2% in the other, higher resolution runs. Improvements in atmosphere handling are thus needed in our code for systems involving vacuum regions (e.g. BH + neutron star mergers). Later on, in Section 4, we show that errors in mass conservation do not affect the results presented in this paper since the relevant dynamics remain completely contained within the gas cloud.

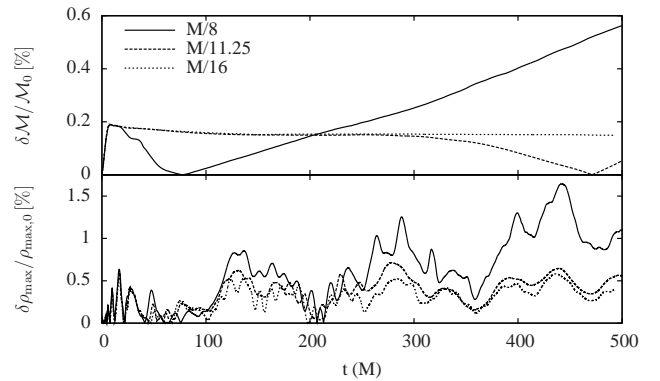


FIG. 1.— Top panel shows the errors in baryonic mass conservation as a function of time from the evolution of a TOV at different numerical resolutions. Bottom panel shows the corresponding errors in the central density.

3. INITIAL DATA

With the uncertainties in our understanding of accretion flow properties around binaries, it is not possible to uniquely define initial conditions for simulations of BBHs and gas on very small scales ($\sim 10^{-5}$ pc), such as those considered in the present work. Nevertheless, the physical properties of the gas in the vicinity of the BHs are likely to be bracketed by two

characteristic scenarios depending on the balance of heating and cooling mechanisms in the accretion flow. In the first scenario, a hot and turbulent accretion flow forms as a consequence of relatively inefficient cooling processes; the BBH is then immersed in a pressure-supported, geometrically thick torus with a scale height H comparable to its radius R . Hereafter, we refer to this scenario as the *gas cloud* model. In the second scenario, relatively efficient cooling processes result in the gas settling into a rotationally-supported, geometrically thin ($H < R$) accretion disk around the binary. This scenario is commonly referred to as the *circumbinary disk* model and has been previously studied by means of non-relativistic hydrodynamic simulations (Armitage and Natarajan 2002; Milosavljević and Phinney 2005; Hayasaki et al. 2007, 2008; MacFadyen and Milosavljević 2008; Cuadra et al. 2009). In this paper, we consider the gas cloud scenario and defer the numerical investigation of the circumbinary disk with a fully relativistic treatment to a future study.

Though the majority of BBHs in the universe are expected to be unequal-mass binaries, we will consider for computational accessibility and as a first step only equal-mass binaries where we can exploit symmetries of the system. Our simulations thus consist of equal-mass binaries with total mass M and initial separation of $R = 8M \approx 10^{-5} M_7 \text{ pc}$, where $M_7 = M/10^7 M_\odot$. This choice of mass scaling yields BBHs which can be detected in the LISA band during the plunge and coalescence and therefore in a regime where modeling is only accessible via NR. As these systems are among the higher mass BBH systems in LISA’s sensitivity window, they are relatively luminous in gravitational radiation and, if associated with an EM signature, likely to be among the most EM luminous binaries that LISA can detect.

The initial data for our simulations consist of a BBH immersed in a gas cloud with a radius of $60M$. The radius of the cloud is selected arbitrarily and in such a way that it entirely encloses the binary orbit. The gas cloud is initially static with a Gaussian density profile

$$\rho = \rho_o e^{-\frac{r^2}{2\sigma^2}} \quad (10)$$

where $\sigma = 10.83M$ and ρ_o is the central density in the cloud. The σ was chosen to avoid non-atmosphere gas densities from reaching the outer boundary initially, though subsequent simulations show larger σ do not change the results qualitatively. The value of ρ_o adopted in our simulations is obtained by extrapolating the results of larger scale simulations that follow the evolution of BBHs in gaseous environment in the aftermath of galactic mergers. These results suggest that the amount of gas which remains strongly bound to the binary on scales of $\lesssim 10^{-2} \text{ pc}$ can be of the order of 1% of the total mass M of the binary (Colpi et al. 2007). This implies a mean gas density of

$$\rho \approx \frac{0.01 M}{(0.01 \text{ pc})^3} \approx 10^{-11} M_7 \text{ g cm}^{-3}. \quad (11)$$

Note that the internal units in the MAYAKRANC code are given in terms of the total mass of the binary, M . For vacuum simulations, this implies that the results from a BBH simulation with mass M can be scaled to arbitrary BH physical masses. For non-vacuum simulations such as those in the present work, the BH mass also determines the scaling of hydrodynamical variables (e.g., density, pressure, internal energy, etc.). In particular, density scales as M^{-2} . Thus, in non-vacuum simulations scaling with M is not arbitrary and

the mass parameter should be chosen in such a way as to reflect a plausible range of densities. We set the initial central density of the gas cloud to $\rho_o = 7 \times 10^{-12} M_7^{-2} \text{ g cm}^{-3}$, a value consistent with the mean density estimate in Eq. 11. The total rest mass of the gas cloud in the computational domain is, initially, $\sim 10^{-4} M_7 M_\odot$, about 11 orders of magnitude lower than the BH masses. For computational facility, we surround the gas cloud with a uniform, low density atmosphere of density $10^{-5} \rho_o$.

We use a polytropic equation of state $P = \kappa \rho^\Gamma$ to construct the initial data; the temperature of the gas is then given by

$$T = \frac{m_p c^2}{k_B} \frac{P}{\rho} = \frac{m_p c^2}{k_B} \kappa \rho^{\Gamma-1}. \quad (12)$$

In this gas cloud model, the thermal energy of the gas is comparable to its gravitational potential energy. Thus, the velocity of the fluid in the vicinity of the BHs is

$$v_{\text{th}} = \sqrt{\frac{3k_B T}{m_p}} \simeq 0.35c \sqrt{\frac{8M}{R}}, \quad (13)$$

where T is the temperature of the gas. It follows that the gas in the vicinity of the binary is a high temperature plasma, $T \sim 10^{12} \text{ K}$, with thermal velocities comparable to the binary orbital speed. We then estimate the adiabatic constant κ in the polytropic equation of state by evaluating Eq. 12 at the center of the cloud, where $T_o = 10^{12} \text{ K}$ and $\rho_o = 7 \times 10^{-12} \text{ g cm}^{-3} M_7^{-2}$, and obtain $\kappa = 2.51 \times 10^8 (\text{cm}^3/\text{g})^{\Gamma-1}$, where $\Gamma = 5/3$. For these values and an ideal fluid equation of state, we find the speed of sound at the center of the cloud,

$$c_s = \sqrt{\frac{1}{h} \left(\frac{\partial P}{\partial \rho} + \frac{P}{\rho^2} \frac{\partial P}{\partial \epsilon} \right)} = \sqrt{\frac{(\Gamma-1)(\epsilon+P/\rho)}{h}} \simeq 0.28c. \quad (14)$$

Because the speed of sound is comparable though smaller than the thermal velocity and the orbital velocity of the binary, it follows that shocks can be expected to develop in vicinity of the BHs.

The gas cloud surrounding the BBH is not in hydrostatic equilibrium. Namely, if the cloud were placed in a potential well of a single BH, the top layers of the cloud would be gravitationally unbound and the gas cloud would expand, doubling its volume over approximately $130M$ of evolution. However, a condition for hydrostatic equilibrium in the case of an isolated BH is of limited utility for the binary scenario considered here. In a realistic case, the binary torques will act to unbind some fraction of gas and, as a result, the outer layers of the cloud in the binary scenario can be expected to be hotter (i.e., less gravitationally bound) compared to the cloud in equilibrium around a single BH. The simple initial conditions we choose emulate this behavior. Note however that in order to achieve more realistic initial conditions one should, in principle, evolve the cloud in the potential of a rotating BBH long before the inspiral and merger until quasi-steady state is achieved. Such relaxation is nontrivial and computationally expensive in the case of a general relativistic system. Instead, we start the evolution of the gas cloud in the initially *frozen*, non-rotating gravitational potential of the BBH for $32M$ of evolution time, or four times the crossing-time of the system. During this phase, the cloud passively evolves to form a gravitationally bound core with two density peaks, each associated with one of the BHs. After this period, we “unfreeze” the binary and evolve it on its orbit for an additional $\sim 60M$ (half

orbit), during which the gas adjusts to the dynamics of the binary. Any transients that develop as a consequence of this initial relaxation are the artifact of imperfect initial conditions and are not considered as a true signature of the system.

The initial distribution of velocity vectors of fluid elements is isotropic about the center of mass of the system. Given the high thermal velocities, it follows that in such a flow, the radial inflow speed of the gas will always be sufficiently high that the binary torques will be incapable of evacuating all of the gas and creating a low density “hole” in the center of the cloud, a property that is a distinguishing feature from the circumbinary disk model. The only mechanisms for heating and cooling of gas in our simulations are adiabatic compression and expansion in the potential of the binary. We do not account for heating of the gas by the active galactic nuclei (AGN) nor for cooling by emission of radiation.

The initial orbital parameters for the BBHs are calculated as though the binary were in vacuum. This is justified since the total mass in the gas cloud is negligibly small compared to the mass of the BHs. We calculate the initial momentum required for quasi-circular orbits from post-Newtonian (PN) equations. For the non-spinning BHs, we evolve the 3rd order PN equations of motion (Buonanno et al. 2006) from a separation of $40M$ to the desired separation. We also consider binaries with spinning BHs where spins are parallel and either aligned or anti-aligned with the orbital angular momentum. In this case we calculate the initial momentum of the BHs from the 3rd-order PN angular momentum found in Eq. (4.7) of (Kidder 1995), assuming purely tangential momenta. Table 1 lists parameters for the BBH systems discussed in this paper. For each BH, labeled 1 and 2, $a_{1,2}/m$ is the dimensionless spin parameter, where m is the mass of each BH set in such a way that $m/M = 1/2$, with M the total mass of the binary. As mentioned before, the BHs are placed at a coordinate distance $8M$ along the x -axis, with BH_1 located at $x = 4M$ and BH_2 at $x = -4M$. In Table 1, P^x and P^y are the components of linear momentum for BH_1 . Finally, m_i is the irreducible mass for the individual BHs computed from the area of their AH, and M_{ADM} is the total initial energy of the system.

The simulations are run on a grid whose outer boundary is located at $317.44M$, with 9 levels of mesh refinement. The 4 coarsest levels are fixed about the center of mass while the 5 finest levels are constructed around and free to follow the BHs. For runs G0, G1, and G3, the finest resolution is $M/51.6$ and the refinement boundaries are chosen such that the 5 finest have radii of 32 grid points while the 4 coarsest have radii of 64 grid points. The mesh setup for G2 was altered somewhat as higher spins require a higher resolution at the puncture. The physical refinement boundaries of G2 remain stationary while the resolution is increased for a finest resolution of $M/67.7$. For all runs, we halve the evolved computational domain by using the reflection symmetry about the xy -plane. For runs G0, G1, and G2, we halve the domain again using rotational symmetry.

4. DYNAMICS OF THE BINARY AND GAS

We now describe the general features and dynamics of the binaries and gas in our modeled systems. BBHs with an initial separation of $8M$ evolve for approximately 3 orbits before they plunge and finally merge. Since the mass of the gas cloud is small compared to the BBH, the binary dynamics are practically indistinguishable from the equivalent situation in

Run	a_1/m	a_2/m	P^x/M	P^y/M	m_i/M	M_{ADM}/M
G0	0	0	-2.0902×10^{-3}	0.11237	0.5000	0.9878
G1	+0.4	+0.4	0	0.10862	0.4893	0.9875
G2	+0.6	+0.6	0	0.10677	0.4736	0.9874
G3	+0.4	-0.4	0	0.11237	0.4893	0.9878

TABLE 1
BBH INITIAL PARAMETERS.

vacuum. The only differences among the cases we considered are due to the “hang-up” or delay induced by the BH spins (Campanelli et al. 2006b). The excess of angular momentum from the BH’s spins result in runs G1 and G2 taking longer to merge compared to runs G0 and G3. In run G2 for example, the hang-up extends the inspiral to about 5 orbits before merger.

In Figures 2 and 3 we show snapshots of the baryonic rest mass density for the cases G2 and G3. The distinct features that arise in the gas during the binary’s evolution are the density waves that develop behind the inspiraling BHs and a bar of high density gas connecting the two BHs. This pattern of density distribution of gas is not unique to relativistic systems and was previously noticed in simulations of binary systems interacting with gas on a variety of scales, including binary galactic nuclei and TTauri stars. In order to examine whether the gas dynamics driven by the binary give rise to shocks, we calculate the Mach number, $\beta_s = v/c_s$, by comparing the velocity of the fluid element to the speed of sound measured locally in the simulation⁵. Figures 4 and 5 show sequences of snapshots with the distribution of the Mach number value for the gas in the plane of the binary of runs G2 and G3. In all of the panels, only transonic and supersonic parts of the flow were plotted, where $\beta_s \geq 1$. Early in the inspiral, the shocks are confined to the density wakes expanding externally to the binary orbit. Later in the inspiral, the bar of high density gas forms between the BHs, and its expansion gives rise to another shock region emanating from the central part of the binary orbit. As the BBH evolves closer to merger, the central high density region decreases in size, being replaced after the merger by a steadier inflow in the immediate vicinity of the final BH.

Here we briefly make a note of the degree to which baryonic mass is conserved in our simulated binary systems, as discussed in the context of a TOV star at the end of §2. We monitor the conservation of mass in two separate volumes: (1) the volume $r \leq 8M$ excluding the regions inside the AHs and (2) the volume $8M \leq r \leq 20M$, external to the binary orbit. This allows us to calculate the total error in mass conservation over the whole computational domain but also to more closely monitor the inner region containing the binary. From run G0 we measure that the baryonic mass is conserved in both volumes at the level of $< 1\%$ over the duration of the simulation. Due to similarities in computational setup and the physical systems, similar mass conservation is expected in the other runs.

5. ELECTROMAGNETIC AND GRAVITATIONAL WAVE SIGNATURES

In this section, we discuss the EM and GW signatures expected to arise from the binary dynamics and accretion flows

⁵ Though $\beta_s > 1$ is necessary, it is not a sufficient condition to locate shocks (e.g., cold fronts). Given the long cooling timescale of the hot, diffuse gas, however, discontinuities in the Mach number within our simulations do select regions where shocks are likely to form.

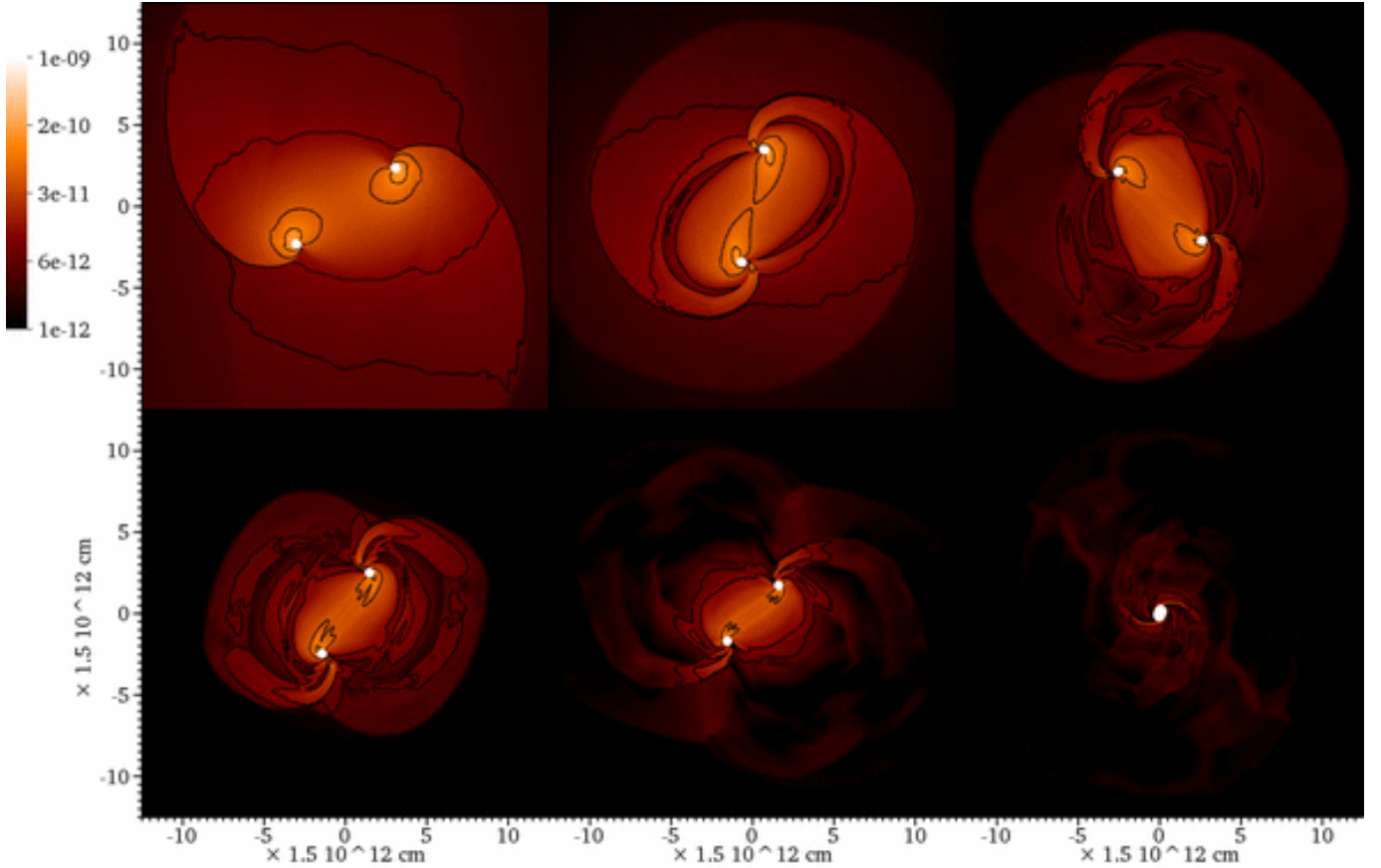


FIG. 2.— Snapshots of the baryonic rest mass density, ρ [g cm^{-3}], in the orbital plane of the binary shown for run G2. From upper left to lower right the snapshots correspond to $t = 7.6 \times 10^2 M_7 \text{ s}$, $1.3 \times 10^3 M_7 \text{ s}$, $1.9 \times 10^3 M_7 \text{ s}$, $2.5 \times 10^3 M_7 \text{ s}$, $3.1 \times 10^3 M_7 \text{ s}$, and $3.7 \times 10^3 M_7 \text{ s}$ respectively. The color scale is logarithmic, with contour lines plotted at half order-of-magnitude intervals.

during the late inspiral, plunge, and merger of the BHs. We analytically estimate the characteristic timescales and emission properties of the hot gas in Section 5.1. In Section 5.2, we evaluate the bremsstrahlung emission from our simulations and compare it to the emission powered by accretion onto the two BHs (Section 5.3). In Section 5.4, we characterize the GW signatures and highlight combined EM+GW signatures that may enable us to distinguish binary systems from isolated BHs. Finally, in Section 5.5 we discuss the observability of coalescences in the gas cloud scenario.

5.1. Characteristic timescales and properties of the gas

We compare the physical properties of the hot plasma in our simulations with the hot flows that are expected to arise in a fraction of AGNs as radiatively inefficient accretion flows (RIAFs). From these characteristic timescales, we find that the gas flow in our simulations in some respects resembles RIAFs. We do not, however, carry out a self-consistent simulation of the multi-component plasma or radiative transfer in such flows as such a detailed treatment would be beyond the scope of this study. The main property of radiatively inefficient flows is that very little energy generated by accretion and turbulent stresses is radiated away, being instead stored as thermal energy in the gas; this gives rise to a very hot flow (Ichimaru 1977; Rees et al. 1982; Narayan & Yi 1994). Since thermal pressure forces within the gas are significant, the hot accretion flows are expected to be geometrically thick. Given high thermal velocities, the inflow speeds in the flow are comparable to the speed of sound and the orbital velocity that a test particle would have at a given radius.

Below some critical gas density, the Coulomb collision time in RIAF-type flows becomes longer than the inflow time of the gas, resulting in a two-temperature flow in which the ion plasma remains at $T_p \sim 10^{12} \text{ K}$ and the electron plasma cools to temperatures in the range $T_e \sim 10^{10} - 10^{12} \text{ K}$. Since electrons are more efficient radiators, the observed radiation will thus be determined by the properties of the electron population. In order to determine whether the hot plasma in the cloud developed a two-temperature flow, we evaluate the characteristic timescales for the inflow of gas t_{inflow} and Coulomb collisions t_{Coulomb} in the vicinity of the binary. We estimate that for the gas cloud under consideration

$$t_{\text{inflow}} \approx 0.4 \text{ hr} \left(\frac{R}{10M} \right) \left(\frac{c_s}{0.3c} \right)^{-1}, \quad (15)$$

$$t_{\text{Coulomb}} = \frac{1}{n\sigma c_s}$$

$$\approx 0.5 \text{ hr} \left(\frac{\rho}{10^{-11} \text{ g cm}^{-3}} \right)^{-1} \left(\frac{c_s}{0.3c} \right)^{-1} \left(\frac{T_e}{10^{10} \text{ K}} \right)^2$$

The size of the region under consideration here, R , is comparable to the Bondi radius of gravitational influence of the BH binary. $n \approx n_p \approx n_e \approx \rho/m_p$ is the number density of the gas, c_s is the speed of sound, ρ is the characteristic density of the cloud, and $\sigma \approx 0.3Z^2e^4/(kT_e)^2$ is the cross-section for Coulomb scattering of an electron with kinetic energy $\sim kT_e$ on a more massive ion, evaluated for a population of electrons with $T_e \sim 10^{10} \text{ K}$.

Because $t_{\text{Coulomb}} \gtrsim t_{\text{inflow}}$ for the gas considered here, we conclude that the gas cloud region can be described as a two

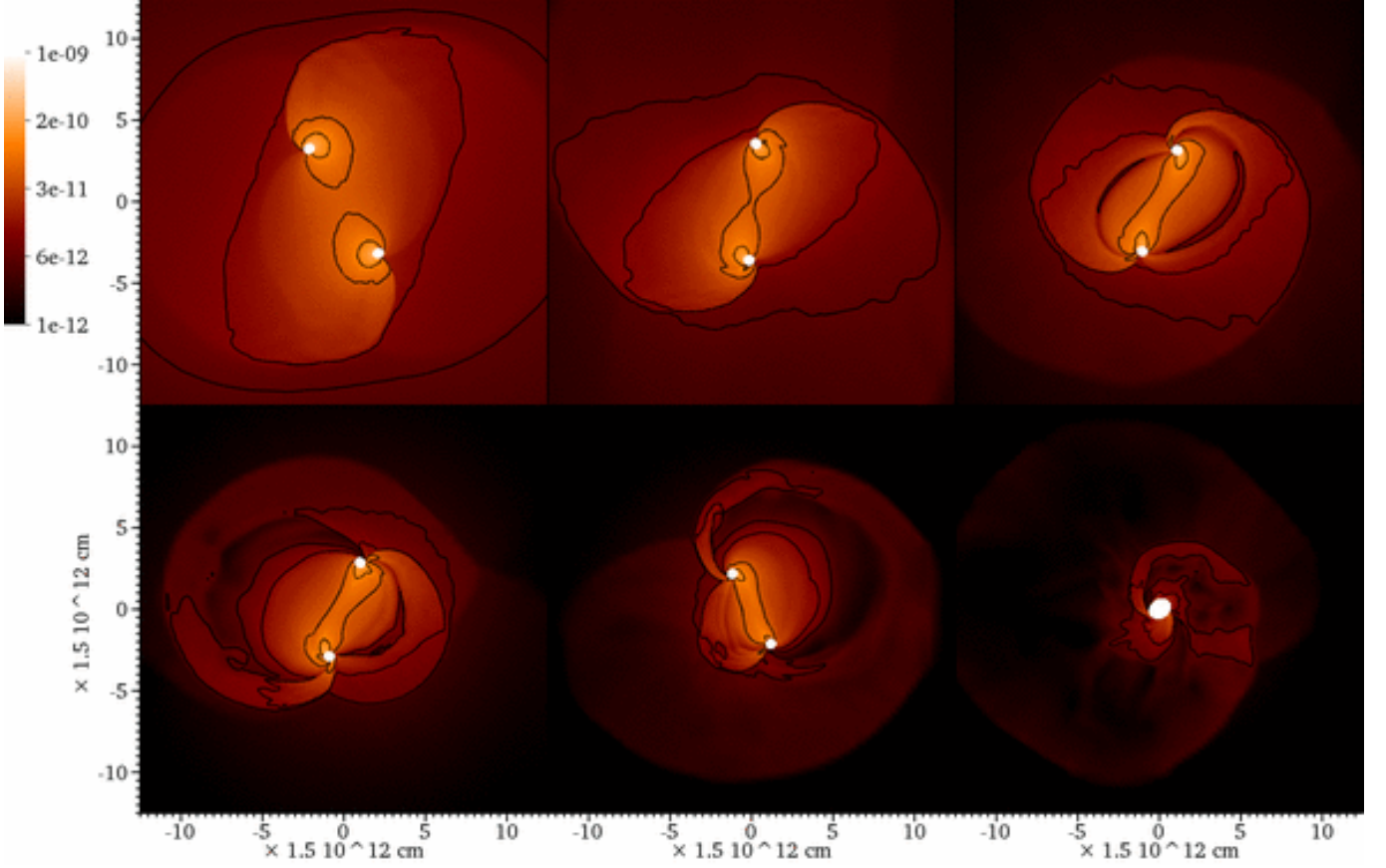


FIG. 3.— Same as in Fig. 2 but for the run G3. From upper left to lower right the snapshots correspond to $t = 3.1 \times 10^3 M_7$ s, $6.2 \times 10^3 M_7$ s, $9.2 \times 10^3 M_7$ s, $1.2 \times 10^4 M_7$ s, $1.5 \times 10^4 M_7$ s, and $1.8 \times 10^4 M_7$ s respectively.

temperature flow with $T_e < T_p$. However, given that the two timescales are not far apart in the center of our cloud, the electrons and ion plasma may remain weakly coupled and, via occasional scattering with ions, electrons near the BHs may largely preserve the thermal energy distribution. Thus, we estimate the bremsstrahlung luminosity from a thermal distribution of electrons (Rybicki and Lightman 1986)

$$L_{\text{brem}} \approx 4 \times 10^{44} \text{ erg s}^{-1} \left(\frac{\rho}{10^{-11} \text{ g cm}^{-3}} \right)^2 \left(\frac{R}{10M} \right)^3 M_7^3 \left(\frac{T_e}{10^{10} \text{ K}} \right)^{1/2} \left[1 + 4.4 \times \left(\frac{T_e}{10^{10} \text{ K}} \right) \right]_{5.4}. \quad (17)$$

where subscript “5.4” indicates that a numerical factor in the square brackets is normalized to 5.4. For comparison, the Eddington luminosity of the system is $L_{\text{Edd}} \approx 1.3 \times 10^{45} \text{ erg s}^{-1}$. We therefore estimate that thermal bremsstrahlung is the dominant emission mechanism of the hot flow, as the synchrotron radiation and inverse Compton scattering are comparably

smaller⁶:

$$L_{\text{synchro}} \approx 8 \times 10^{36} \text{ erg s}^{-1} \left(\frac{\rho}{10^{-11} \text{ g cm}^{-3}} \right) \left(\frac{R}{10M} \right)^3 \left(\frac{B}{1G} \right)^2 M_7^3 \quad (18)$$

$$L_{\text{IC}} \approx 3 \times 10^{-8} L_{\text{soft}} \left(\frac{\rho}{10^{-11} \text{ g cm}^{-3}} \right) \left(\frac{R}{10M} \right)^3 \left(\frac{R_{\text{tran}}}{10^5 M} \right)^{-2} M_7 \quad (19)$$

where the relativistic factor $\beta = v/c$ and Lorentz factor W have been evaluated for $v/c \approx 0.3$. Here L_{soft} is a supply of low energy photons transported from the edge of the RIAF, a distance of R_{tran} away.

Note that the luminosity of the synchrotron emission remains below that of the bremsstrahlung radiation unless the magnetic field strength is close to the equipartition value, which in our case is $B_{\text{equip}} \sim 10^5 G$. Because our simulations are purely hydrodynamical, we have no means of constraining the magnetic field strength and its dynamics around the coalescing binary. Thus in estimating L_{synchro} , we have assumed that magnetic fields are sufficiently weak and that the synchrotron component is not the dominant one.

Similarly, in order for the inverse Compton luminosity to be significant, a supply of soft, lower energy photons, presu-

⁶ Synchrotron and inverse Compton scattering luminosities were derived from the standard expressions; see (Rybicki and Lightman 1986), for example.

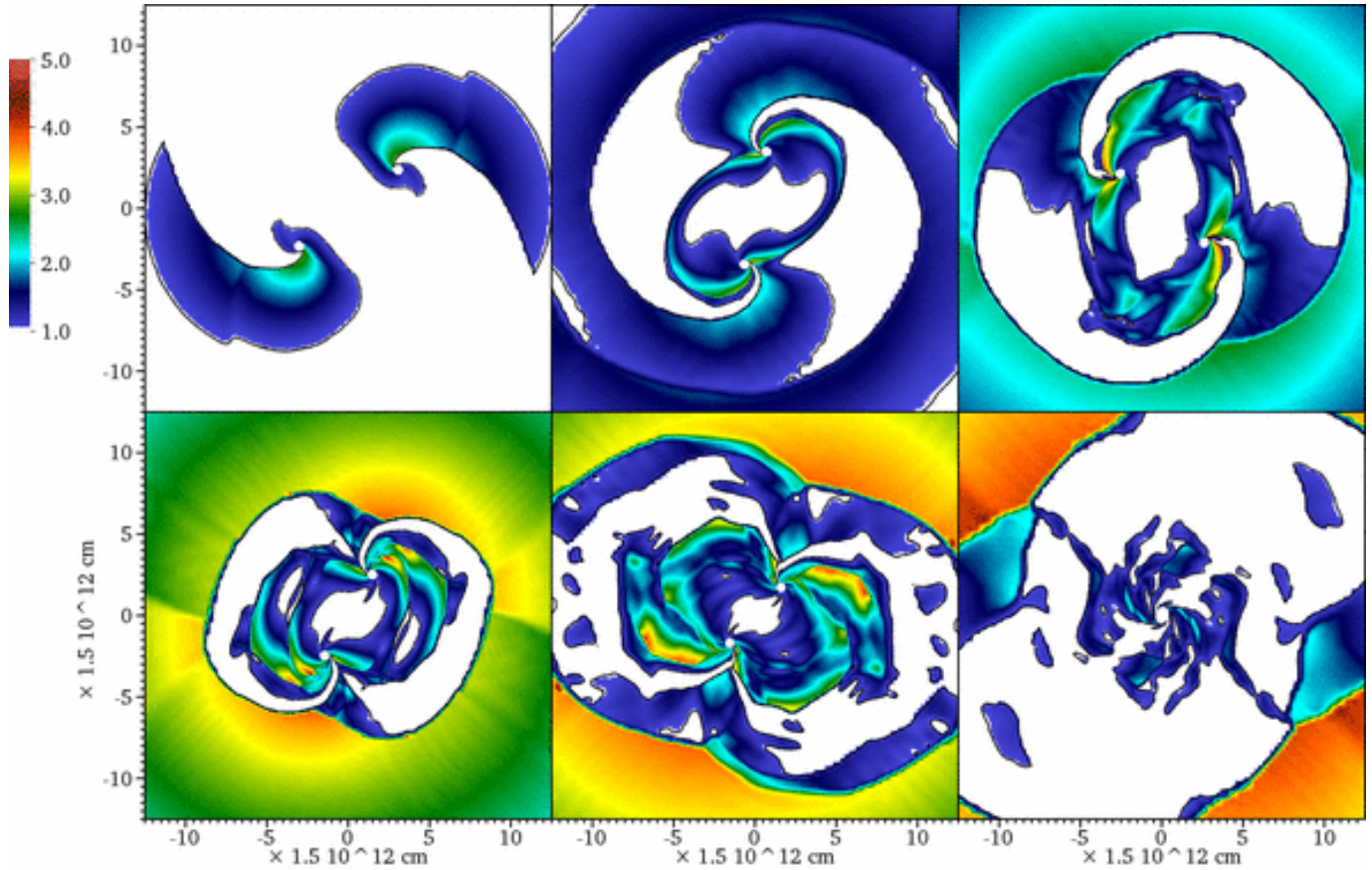


FIG. 4.— Snapshots of the Mach number, $\beta_s = v/c_s$, measured in the orbital plane of the binary in run G2, shown at the same times as in Fig. 2. Only values $\beta_s \geq 1$ are shown. The color scale is linear ranging from light (blue) for $\beta_s = 1$ to dark (red) for $\beta_s = 5$, with the black contour line marking the location of $\beta_s = 1$.

ably produced externally to the hot binary accretion flow, is required. In estimating L_{IC} , we assumed that this soft photon component is produced at large radii, where radiative cooling is efficient and the geometrically thick flow described here transitions into a geometrically thin accretion disk or a lower temperature ambient medium. In the case of Sgr A* for example, observations indicate that a radiatively inefficient accretion flow extends into the ambient medium out to distances $R_{\text{tran}} \sim 10^5 M$ away from the center (Quataert 2003). The estimate for L_{IC} obtained with this value of the transition radius implies that inverse Compton scattering is a very inefficient process even if a generous supply of low energy photons is available from the ambient medium, parametrized here in terms of the luminosity L_{soft} .

Note that a subsequent paper to the current work (Farris et al. 2009) suggests that the spinning BHs could amplify the magnetic fields in their vicinity by several orders of magnitude to nearly the equipartition value. In the context of a scenario considered by Farris et al. (2009), where the magnetic field strength is about an order of magnitude less than at equipartition (i.e., $B \sim 10^4 G$ given the properties of our gas cloud), the estimate for luminosity of synchrotron radiation becomes $L_{\text{synchro}} \sim 10^{45} \text{ erg s}^{-1}$ (see equation 18). In this scenario, not only is L_{synchro} comparable to L_{brem} , but the synchrotron radiation could feed the inverse Compton luminosity of comparable magnitude (equation 19) by providing an immediate source of soft photons. In the present work, however, we have no means of judging the strength of the magnetic field in the immediate vicinity of the binary and we focus most of our discussion on bremsstrahlung emission, keeping in mind the potential importance of the other two emission

mechanisms.

The corresponding cooling timescale of the plasma at $T_p \sim 10^{12} \text{ K}$ due to bremsstrahlung radiation from $T_e \sim 10^{10} \text{ K}$ electrons is

$$t_{\text{cool}} \sim 8 \text{ hr} \left(\frac{\rho}{10^{-11} \text{ g cm}^{-3}} \right)^{-1} \left(\frac{T_p}{10^{12} \text{ K}} \right) \left(\frac{T_e}{10^{10} \text{ K}} \right)^{-1/2} \quad (20)$$

Note that $t_{\text{cool}} > t_{\text{Coulomb}} > t_{\text{inflow}}$ implies that the hot gas plunges into the BHs before it had a chance to radiatively cool and settle into an accretion disk, thus justifying the initial assumption of a hot, geometrically thick gas cloud and implying that radiative cooling of the cloud can indeed be neglected in this case. It is also worth noting that the expressions presented in this section scale with density and thus can be used to estimate luminosity components from a lower density plasma than that considered here. The scaling relations however break down for plasma densities higher than $10^{-11} \text{ g cm}^{-3}$ because in this regime Coulomb collisions become sufficiently frequent as to thermalize the electrons and produce a single temperature plasma flow. Once the plasma flow of electrons and ions is fully thermally coupled, it can cool efficiently via electron-emitted radiation, yielding an evolution more similar to the accretion disk scenario.

5.2. Bremsstrahlung emission from the gas

We now evaluate the characteristic luminosity arising from the gas near the BBH in our simulations. At a given time step during the simulations, we calculate the local thermal bremsstrahlung emissivity $\mathcal{E}_{\text{brem}}$ (i.e., luminosity per unit vol-

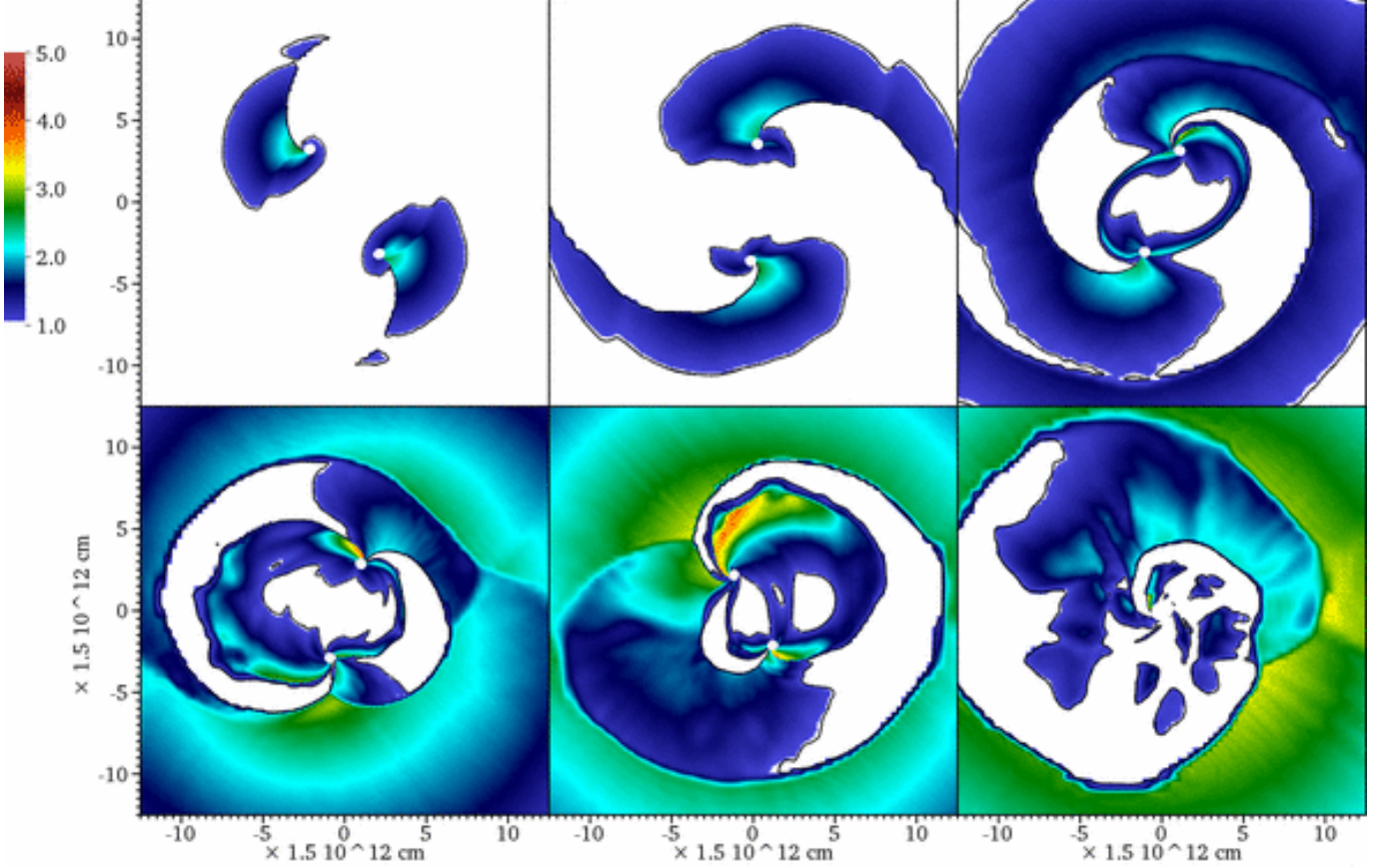


FIG. 5.— Same as in Fig. 4 but for the run G3.

ume) from Rybicki and Lightman (1986) as

$$\mathcal{E}_{\text{brem}} = 2.8 \times 10^4 \text{ erg s}^{-1} \text{ cm}^{-3} \left(\frac{\rho}{10^{-11} \text{ g cm}^{-3}} \right)^2 \left(\frac{T_e}{10^{10} \text{ K}} \right)^{1/2} \left[1 + 4.4 \times \left(\frac{T_e}{10^{10} \text{ K}} \right) \right]_{5.4}, \quad (21)$$

where we assumed that $T_e = 10^{-2} T_p$, with T_p computed from the internal energy ϵ in our simulations as

$$\frac{k T_p}{m_p c^2} = (\Gamma - 1) \epsilon. \quad (22)$$

Figures 6 and 7 show snapshots of the bremsstrahlung emissivity $\mathcal{E}_{\text{brem}}$ for the gas located in the plane of a binary in runs G2 and G3. The time sequences of the snapshots correspond to those in Figs. 2 – 5 for the density and Mach number. Not surprisingly, the highest bremsstrahlung emissivity is found in the regions of high density, namely at the wakes trailing behind the BHs and, at later times, around the central bar of gas between the BHs. By comparing Figure 6 (emissivity) with Figure 4 (Mach number) in runs G2 and G3, it is evident that regions of high emissivity are closely associated with regions where shocks arise and expand into the surrounding cloud. In the late stages of the merger, most of the emission is produced by the bridge of shocked gas between the BHs. This region decreases in size as the BHs approach coalescence and is rapidly swallowed by the BHs when they merge to form a single, final BH. As we will discuss next, this gives rise to a characteristic variability in the bremsstrahlung light emitted by the gas.

To obtain the bremsstrahlung luminosity L_{brem} , we integrate $\mathcal{E}_{\text{brem}}$ over a spherical volume of radius $10M$, enclosing the binary orbit but excluding the volumes inside the AHs. By repeating this procedure at regular time intervals during the simulations, we construct a light curve for thermal bremsstrahlung. Figure 8 shows the light curves for all four runs. In this and subsequent figures, $t = 0$ marks the time when we first find the AH of the final BH. We estimate that the actual merger, i.e. first appearance of a common AH, takes place within $5 \times 10^2 M_7 \text{ s}$ before this.

We first discuss the light curves in Figure 8 represented by solid lines. During the early part of the inspiral, $t \lesssim -5 \times 10^3 M_7 \text{ s}$, the luminosities in all systems decay from the Eddington luminosity level to few $\times 10^{44} \text{ erg s}^{-1}$. At about $t \sim 5 \times 10^3 M_7 \text{ s}$ before the merger, when the binary enters the final plunge, the luminosity starts increasing, leading to a broad flare lasting until the binary merges. The flare reaches its maximum during $-5 \times 10^2 M_7 \text{ s} \lesssim t \lesssim 0 \text{ s}$, a period where we estimate the AHs of the two BHs merge. We measure the maximum luminosity of the flare in G0, G1, G2 and G3 run to be $L_{\text{brem}} = \{15.5, 7.56, 4.96, 13.7\} \times 10^{44} \text{ erg s}^{-1}$, respectively, and estimate the error associated with these measurements to be between 5 and 10%. Our measurements give a lower limit with errors arising because the volume integrated luminosity depends on the formation and geometry of the “common,” final AH, whose early distorted (peanut-like) shape is difficult to localize immediately after its formation. As mentioned before, we estimate that the common, final AH forms during $-5 \times 10^2 M_7 \text{ s} \lesssim t \lesssim 0 \text{ s}$. For this reason, we do not include in Fig. 8 luminosities during this time interval.

Another characteristic feature in the luminosity curves de-

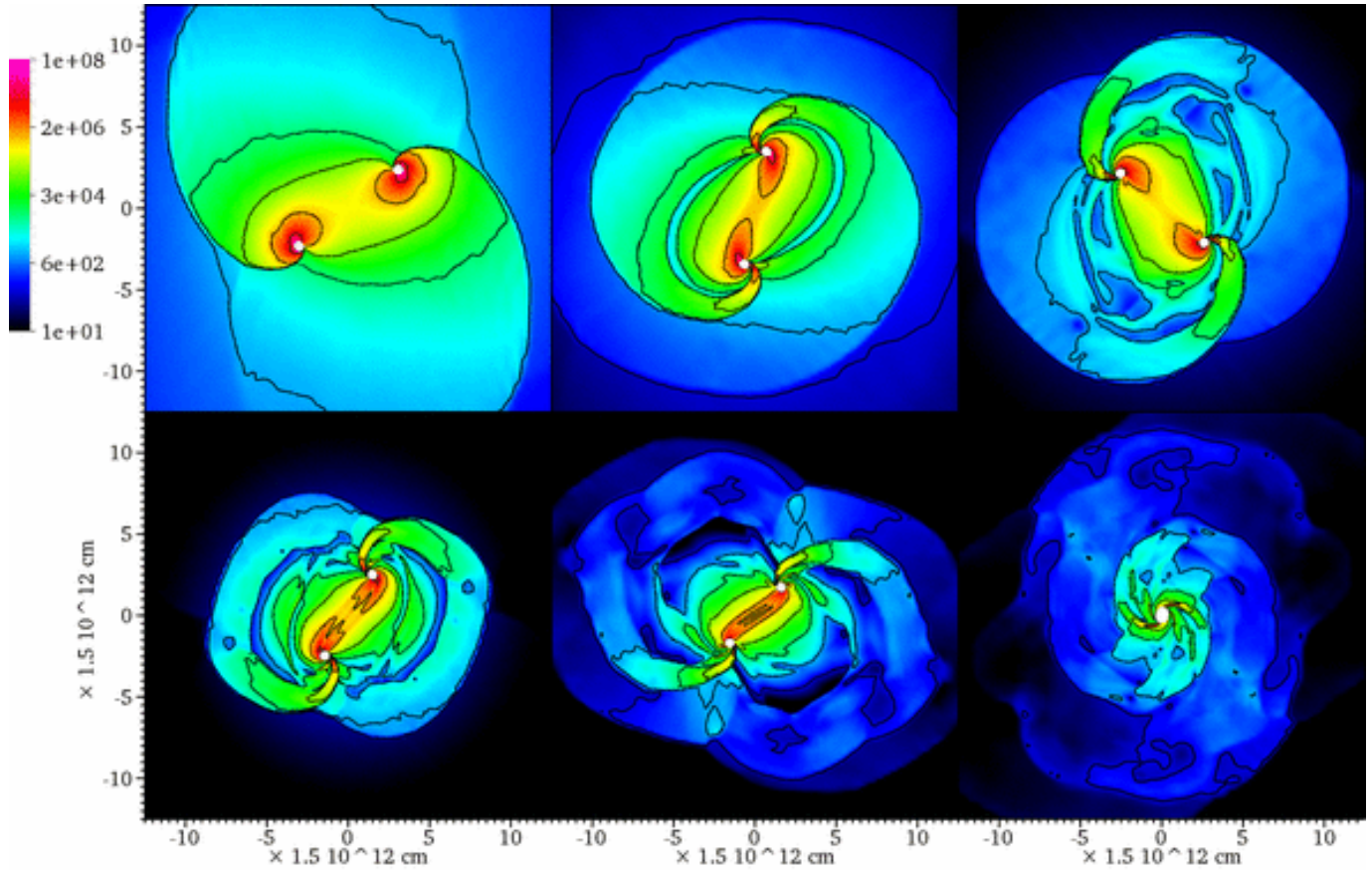


FIG. 6.— Snapshots of the bremsstrahlung emissivity, in units of $[\text{erg s}^{-1} \text{cm}^{-3}]$, shown in the orbital plane of the binary for run G2. The time sequence of snapshots corresponds to Figures 2 and 4. The color scheme is logarithmic and contours are plotted at half order-of-magnitude intervals.

pictured in Figure 8 is a sudden drop that occurs soon after the BHs have merged. This feature is most dramatic in run G1 where the luminosity decreases by nearly 3 orders of magnitude. A sudden decrease can be attributed to the disappearance of the dynamic region of high emissivity between the two BHs, which is rapidly swallowed by the BHs in the process of coalescence.

In all cases, the luminosity eventually decays exponentially. The luminosity in runs G0 and G1 decay in this manner immediately after merger, but runs G2 and G3 exhibit an additional variability before the exponential decay. This exponential decay is due to the steady state accretion of the left-over gas surrounding the final BH.

Since $L_{\text{brem}} \propto \rho^2$, any density variations within the emitting volume are mirrored in the calculated luminosity curve. The variability following the luminosity drop in runs G2 and G3 is especially interesting since it results in a more gradual drop and also highlights some differences in the evolution of the gas in these two runs with respect to runs G0 and G1. Specifically, in run G2, which is the longest of the four runs, the spiral wakes trailing behind the BHs have sufficient time to interact with each other, and, as a result, the final BH finds itself embedded in a highly turbulent medium. Because turbulence heats the gas and creates density inhomogeneities in the cloud, this gives rise to the variability observed in the aftermath of coalescence. Similarly, in run G3, the asymmetry of the system seeded by the prograde and retrograde spinning BHs, leads to interactions of the spiral wakes early in the simulation and gives rise to turbulence and excess luminosity after the coalescence. Since the medium surrounding the binary can be expected to be turbulent in realistic cases, we argue that

realistic light curves may resemble runs G2 and G3 more than cases G0 and G1. Namely, we expect that turbulence would arise naturally in simulated systems that have been evolved for a longer period of time before the coalescence.

We now highlight additional features of bremsstrahlung light curves that arise when relativistic beaming and Doppler boosting are included in the calculation of luminosity (see the curves plotted with dashed lines in Fig. 8). For simplicity, we neglect relativistic bending of photon trajectories and gravitational redshift of photons in the potential well of the binary. We include the special relativistic Doppler effect by multiplying the broadband bremsstrahlung emissivity $\mathcal{E}_{\text{brem}}$ with the factor $D^4 = (W(1 - \beta \cos(\theta)))^{-4}$ where θ is the angle between the line-of-sight to the observer and the velocity vector of the gas. It follows that, depending on the position of an observer relative to the orientation of the binary, the changing beaming pattern of the orbiting binary surrounded by emitting gas can potentially give rise to modulations in the observed luminosity of the system. To judge the importance of this effect, we evaluate the bremsstrahlung luminosity for a configuration in which the modulations are expected to be largest by placing a fiducial observer in the plane of the binary at infinity. In this way, the observer is placed directly in the path of the sweeping emission beams associated with the two BHs and can sample both the minimum and maximum luminosity of the system, depending on its orbital phase. As shown in Fig. 8, see dashed lines, quasi-periodic oscillations in luminosity indeed arise in runs G0, G1, and G2 prior to coalescence. The amplitude of the variations in luminosity is approximately a factor of 2 between subsequent peaks and troughs, oscillating about a value

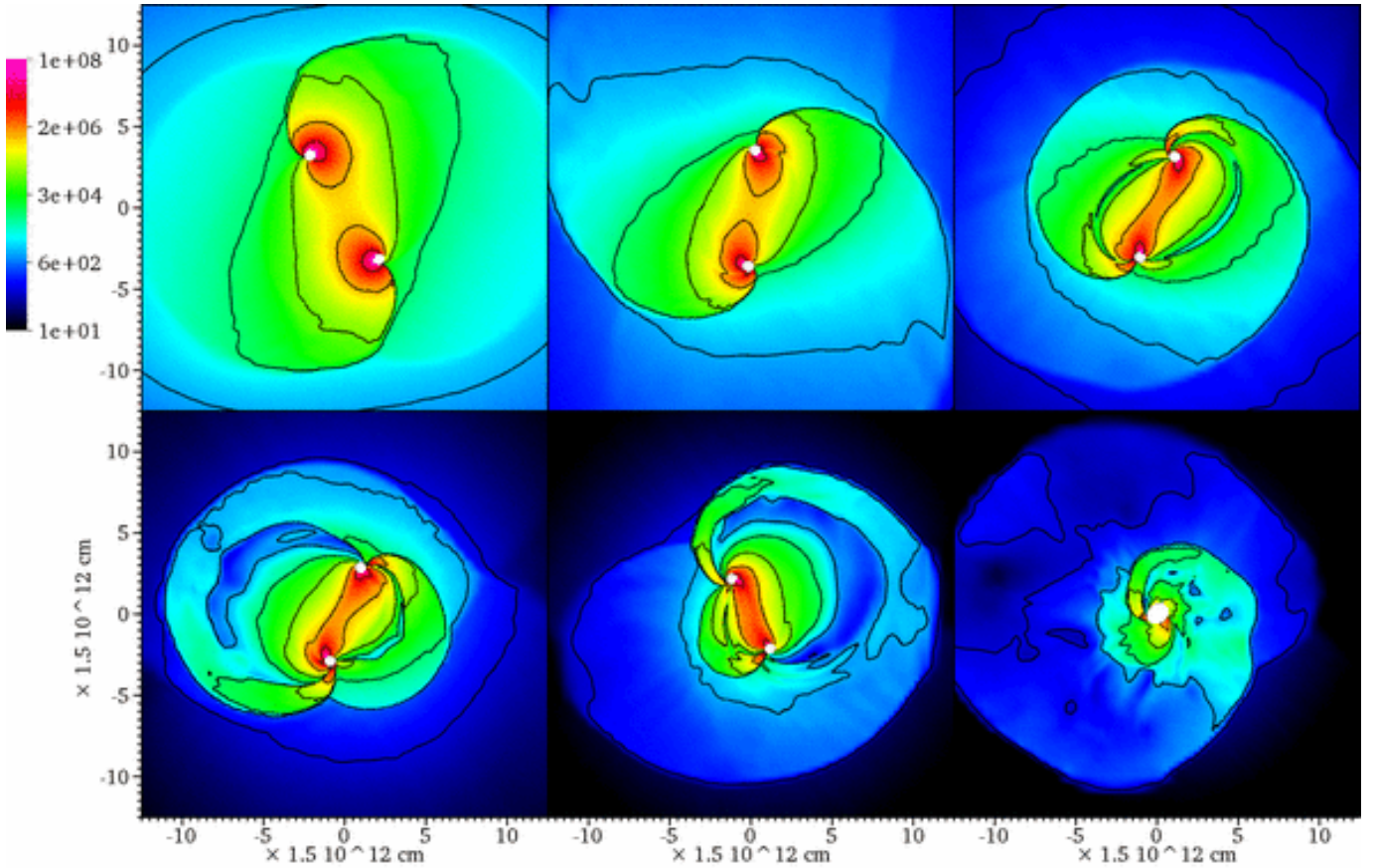


FIG. 7.— Same as in Fig. 6 but for the run G3. The time sequence of snapshots corresponds to Figures 3 and 5.

lower than the unboosted luminosity as boosting into the gas frame reduces the energy of the emitted photon by a factor W^{-1} . Furthermore, it is the beamed emission from the shocks, launched by the BHs into the surrounding layers of the cloud, that contribute the most to the modulation of luminosity. This argument is strengthened when oscillations in runs G0, G1 and G2 are compared with those in the asymmetric case, G3, where the binary does not form a stable set of density wakes. As a result, the luminosity oscillations in run G3 are much weaker (not easily discernible in Fig. 8) and appear at roughly half the frequency seen in the other cases.

The discussed variability stands a chance of being seen by a distant observer, as long as photons emitted in the vicinity of the BHs are not absorbed within the cloud and the surrounding medium or reprocessed in such a way that the variability signature is lost. To estimate these effects, we consider separately the optical depth in the portion of the gas which serves as the source of bremsstrahlung photons and the remainder of the gas cloud. Assuming that the electron population at a temperature $T_e \sim 10^{10}$ K will give rise to a range of photon energies up to $kT_e \sim 1$ MeV, we estimate the optical depth for Compton scattering as $\tau_{\text{Compton}} \approx n\sigma_T R$. For simplicity we replaced the cross-section for Compton scattering by that for Thomson scattering and neglect a factor of few discrepancy between the two that arises for the highest energy photons. Within the emitting portion of the cloud, approximately the central $10M$ or 10^{-6} pc of the system, the number density of the gas cloud ranges from $10^{12} - 10^{15} \text{ cm}^{-3}$ resulting in an optical depth of the order $10 - 10^4$. By contrast, the number densities outside this region drop to order 10^{11} cm^{-3} and below, implying an optical depth of order unity and smaller. There-

fore, if the photon escapes the region of emission it is likely that the variability in luminosity can be seen by an observer.

5.3. Accretion onto the black holes

In this section we discuss the properties and structure of the accretion flows modeled in our simulations. Fig. 9 shows the accretion rates measured across the apparent horizons of the BHs. The dash-dot lines at $t < 0$ s mark the accretion rates onto the individual BHs before the merger. Since the accretion rates of the inspiraling BHs in runs G0, G1 and G2 are identical, only one curve is visible. In run G3, the dash-dot line at $t < 0$ s marks the accretion rate for the prograde spinning BH and the dotted line that of the retrograde spinning BH (prograde direction is defined as a spin parallel to the orbital angular momentum). In all runs, the solid line represents the sum of the accretion rates of the two BHs before the merger and the accretion rate onto the final BH after the merger.

It is prudent here to separate any effects on the accretion rate that stem from our simple assumptions about the initial structure of the gas cloud from physical effects that arise as a consequence of the binary dynamics. To do so we consider the evolution of the same gas cloud, replacing the BBH by a single stationary BH with a mass of $1M \simeq 10^7 M_\odot$ and spin $a/M = 0.62$. This choice of mass and spin approximates the final BH in the G0 case. We overlay the accretion rate for this single BH case and the binary runs in Fig. 10 leaving the time axes unshifted such that the starting moment of each simulation coincides (not the moment of coalescence as in previous figures), again omitting the initial transients. In all cases, the average gas density in the center of the gas cloud decreases exponentially as the gas cloud of finite size is swallowed by

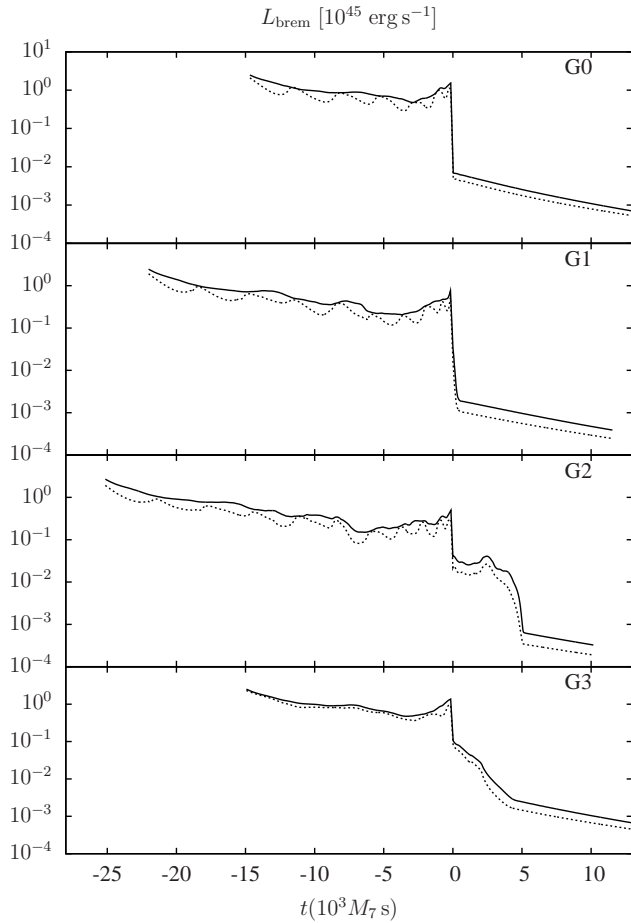


FIG. 8.— Thermal bremsstrahlung luminosity as a function of time without (solid line) and with relativistic beaming (dashed line), calculated within a sphere of radius $10M$ about the center of mass of the binary but excluding the region within the AHs. Effect of beaming is calculated for an observer placed at infinity, in the orbital plane of the binary. Merger occurs at $t \sim 0$.

the BHs. This decline is a consequence of our choice of initial conditions and should not be regarded as a prediction of the simulations, as in reality gas may be continuously supplied to the BH and a leveled accretion rate maintained over longer periods of time. On the other hand, the excess variability in accretion rate noticeable in the four binary scenarios is a consequence of the binary motion which stirs the gas, causing turbulence. It is this variability that we regard as a true signature of the binary.

The two orbiting BHs accrete from a hot, turbulent flow in a Bondi-like fashion. We measure the total accretion rate of the BHs in the simulations to be in the range $0.2 - 2M_{\odot} \text{ yr}^{-1}$, in good agreement with the analytic expectation for Bondi accretion rate of this system

$$\dot{M}_{\text{B}} \approx 0.84 M_{\odot} \text{ yr}^{-1} \left(\frac{c_s}{0.3c} \right)^{-3} \left(\frac{\rho}{10^{-11} \text{ g cm}^{-3}} \right) M_7^2, \quad (23)$$

where we assumed that the relative velocity between the gas and the BH is comparable to c_s . At this rate of accretion, the gas residing in the nuclear region of size $\lesssim 0.01$ pc and mass 1% of the BH's mass will be accreted in $\sim 10^5$ yr. In order for the gas flow to persist uninterrupted on longer time scales, gas needs to be supplied from larger radii, either via an accretion disk or by accretion from the interstellar medium.

A time scale of $\sim 10^5$ yr is, in principle, long enough for the angular momentum of the accreted gas to have an ef-

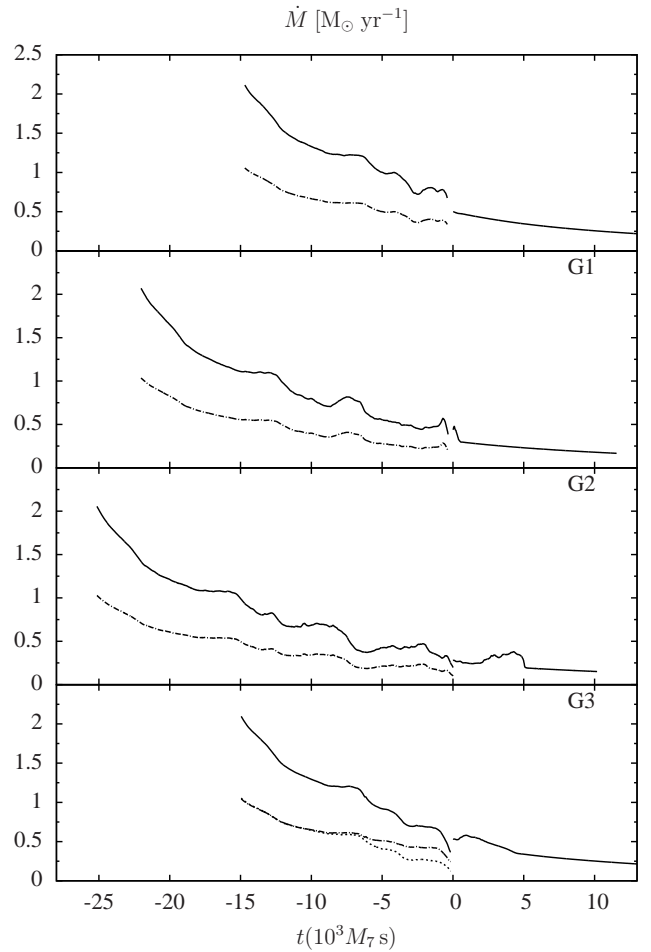


FIG. 9.— Accretion rates across the AHs. Dash-dot lines mark the accretion rates onto individual BHs before the merger, $t < 0$. Accretion curves of pre-merger BHs in runs G0, G1, and G2 overlap due to identical accretion rates. In G3, the dash-dot line marks the accretion rate onto the prograde-spinning BH and the dotted line marks the accretion onto the retrograde-spinning BH. In all cases solid line shows the total accretion rate of the system onto the AHs. Merger occurs at $t \sim 0$.

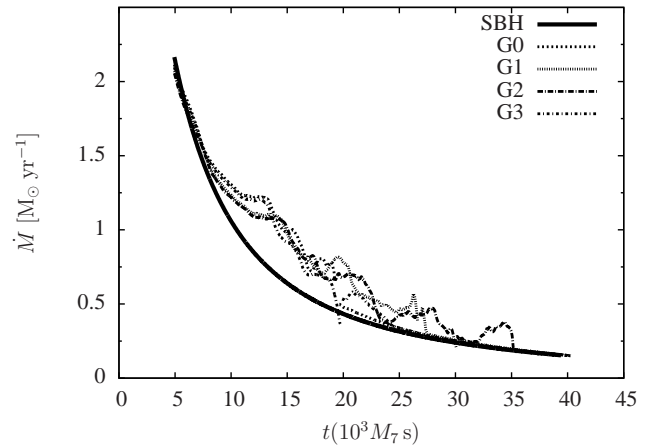


FIG. 10.— Accretion rate of gas onto the single spinning BH (solid line) and the total (sum of individual BH) accretion rates for the binary runs G0-G3 (dashed lines), again omitting the initial transients.

fect on the orientation of the BH spins⁷. Such coupling be-

⁷ Note that in the reference frame co-rotating with the binary the gas has a rotational velocity component, even though its velocity distribution is initially

tween the angular momentum of the accreted gas and the BH rotation can lead to precession of their spin axes and possibly a partial alignment with the orbital angular momentum of the binary. This effect, however, is expected to be more efficient in accretion disks of small and moderate thickness (Natarajan and Pringle 1998; Natarajan and Armitage 1999; King et al. 2005; Lodato and Pringle 2006, 2007; Fragile et al. 2007; Bogdanović et al. 2007; Perego et al. 2009; Dotti et al. 2009). Since the time scale over which we follow the binary and gas in our simulations is much shorter, we capture no spin alignment effects in our study and the BBH dynamics in all of our simulations is essentially indistinguishable from the equivalent vacuum case.

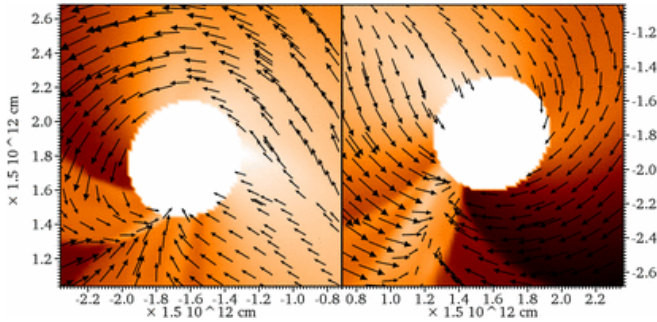


FIG. 11.— Velocity field of the gas plotted in the vicinity of the prograde-BH (left) and retrograde-spinning BH (right) $\sim 3.3 \times 10^3 M_7 s$ before merger, at a point at which the accretion rates differ by a factor of ~ 2 .

Since the BHs in our simulations accrete in a Bondi-like fashion, the expectation is that they draw matter from a region enclosed within their Bondi radius, $R_B = GM/c_s^2$, which approximately delineates the zone of gravitational influence of a BH. While the Bondi radius does not explicitly depend on the spin of a BH, we find from run G3 that the spin orientation of the merging BHs does affect their accretion rates. In G3, the rates of accretion of the two BHs start diverging from each other at approximately $\sim 6.4 \times 10^3 M_7 s$ before the coalescence and reach a factor of ~ 2 difference at the plunge. This difference arises as a combination of the frame dragging and geometry of the density wakes in the vicinity of the BHs. The panels in Fig. 11 highlight the differences in the velocity field of the gas around the prograde- and retrograde-spinning BHs at a time, $\sim 3.3 \times 10^3 M_7 s$ before merger, when the difference in accretion rates is highest. Due to the orbital motion of the binary, the relative motion of the gas flow in Fig. 11 appears to be from right to left at the position of the prograde-spinning BH and from left to right for the retrograde-spinning BH. A fraction of the gas near each BH tends to co-rotate with the spin of the BH. For both BHs the effect of frame dragging is such that the relative velocity of the gas with respect to the BH is effectively lower just below the BH and higher just above it, when compared to the mean velocity of the flow. This low velocity spot is, according to Eq. 23, where most of the accretion is favored to occur across the AHs of the BHs. In the case of the prograde-spinning BH, some of the gas plunges directly into the BH and some rotates around and is fed to it through the trailing wake. In the case of the retrograde-spinning BH, the gas is compressed into the front of the density wake which is then less effective at channeling the gas into the BH, leading to the lower accretion rate visible in Fig. 9. Nevertheless, given the relatively weak implicit

chaotic in the frame of the observer.

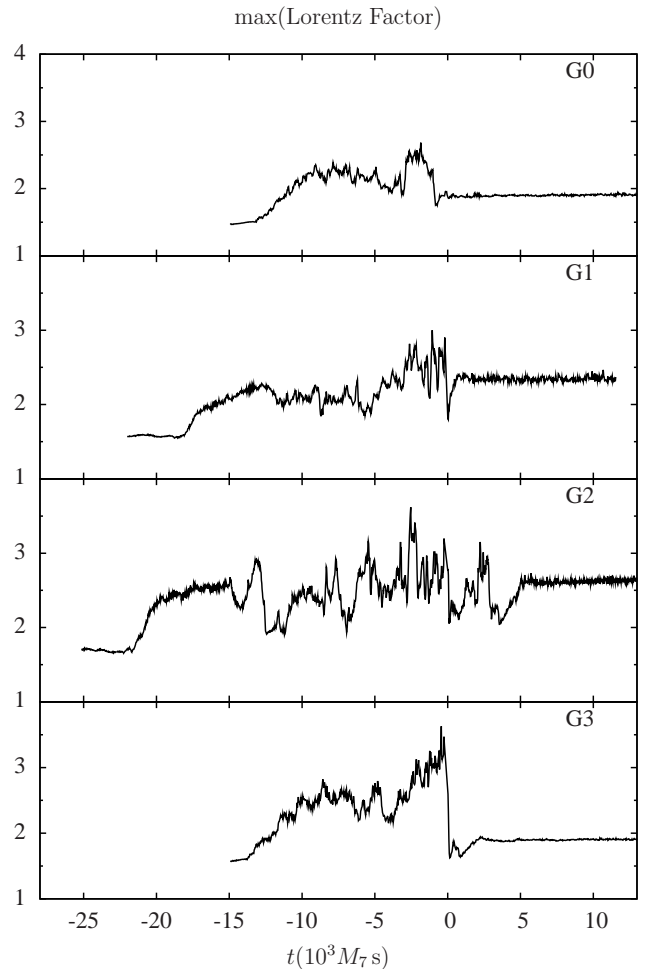


FIG. 12.— Maximum Lorentz factor of the gas outside the AHs. Post-merger values correspond to a steady Bondi-like accretion. Merger occurs at $t \sim 0$.

dependence of the Bondi accretion rate on the BH spin, it is unlikely that one would be able to infer the spin magnitude or orientation in this mode of accretion based on the accretion powered luminosity curve alone.

The discontinuities in the accretion rates observed in Fig. 9 at the time of merger occur due to the error in locating the common, initially highly deformed, AH of the final BH. This is the same source of error that we discussed in the context of the maximum bremsstrahlung luminosity measured at merger time. Notice that for $t > 0$, the exponential decay in the bremsstrahlung luminosity is also mirrored here as an exponential decay in the accretion rate of the final BH. Similarly, the post-merger variability present in runs G2 and G3 (Fig. 8) is also repeated in the accretion rates. As in the case of the luminosity, this behavior can be explained by the more turbulent flows of runs G2 and G3. It is also evident that the accretion rates measured in runs G1 and G2 fall below that in run G0. Since the orbital hang-ups of runs G1 and G2 result in a longer inspiral, the two BHs have more time to deplete the surrounding cloud of gas, leading to a lower density of gas in the vicinity of the binary and consequently lower accretion rates at later times. This is also consistent with the behavior of the bremsstrahlung luminosity curves which are, during the post-merger phase of exponential decay, lower for the spinning-BH cases which exhibit a hang-up, G1 and G2, than for the non-spinning case G0. While details of the exponential decay phase can be dependent on our choice of initial

conditions and the structure of the cloud, the result that systems with a higher net spin magnitude may appear dimmer with respect to their non-spinning counterparts is likely to be real. Without a knowledge of the gas density in the vicinity of SMBH binaries, though, it would be hard to infer the net value of the spin for a given system based solely on the inferred accretion curve.

We now briefly discuss our results in the context of earlier works that considered binary coalescence in non-vacuum, specifically that of van Meter et al. (2009). We compare the global maximum Lorentz factor of the gas calculated from our simulations (Fig. 12) with that in Fig. 2 of van Meter et al. (2009), corresponding to their case where test particles have a random and isotropic velocity distribution.⁸ Since it is likely that the maximum Lorentz factor is found in the immediate vicinity of the BH horizons, in Fig. 12, we do not include the maximum Lorentz factor during $-5 \times 10^2 M_7 s \lesssim t \lesssim 0 s$ because of, as mentioned before, the uncertainty in determining the region outside the final AH.

We find that the maximum Lorentz factors measured for the non-spinning and spinning binary cases during the inspiral phase appear in good qualitative agreement in our respective works. In our simulations, the ramp-up in the Lorentz factor during the inspiral and up to coalescence is reflected in the broad peak in bremsstrahlung luminosity for all runs, thus confirming that the increase in bremsstrahlung luminosity is due to shocks that arise in the vicinity of the binary. Moreover, we confirm that the spinning systems (G1 and G2 cases), on average, have a higher maximum Lorentz factor than the non-rotating G0 case. This behavior can be explained as follows: in the case of spinning BHs, the fluid can travel deeper into the potential well of a BH without being accreted; as a consequence, the fluid can emerge with a higher kinetic energy compared to the non-spinning case. This interpretation is correct as long as the fluid moves freely along a geodesic and before it encounters pressure forces from the surrounding medium. We, however, do not find that overall higher Lorentz factors in the merger of rotating BHs result in higher luminosities. This is because the spinning BHs tend to deplete their surroundings of gas more readily during the orbital hang-up phase and, in such a way, suppress the luminosity.

Unlike van Meter et al. (2009), we do not see a stronger pre-merger spike in the maximum Lorentz factor for the spinning BH cases. We think that this difference can be explained in the context of gas pressure forces. Namely, in the test particle treatment considered by van Meter et al. (2009), pressure gradients are not taken into account and each particle moves along a geodesic with an unaltered velocity. In our work, pressure forces from the surrounding gas act to modify the velocity of the fluid and, in the specific case described above, result in a lower Lorentz factor. This can be seen in Figs. 13 and 14, which illustrate the dynamics of the gas in the immediate vicinity of the binary. During the inspiral, the motion of the binary leads to an ejection of gas which collides with the gas falling inwards, towards the binary. Because the ejected gas is unable to proceed further on its outward radial trajectory and is still within the gravitational influence of the binary, it eventually falls back towards the BHs. In run G2, the gas is being ejected out by the binary on several occasions, giving rise to a turbulent motion in the gas cloud. In run G3 the dynamics

of the flow seeded by the prograde- and retrograde-spinning BHs results in a lopsided ejection-infall event. In both cases this dynamically steered turbulence persists after the merger, leading to the post-merger variability in the bremsstrahlung luminosity and accretion rates.

It is also worth noting that we find somewhat higher maximum Lorentz factors in the post-merger phase compared to the equivalent scenario in van Meter et al. (2009), because our Lorentz factors reflect the bulk inflow of the gas into the merged BH, after the flow settles into a state of steady Bondi-type accretion.

5.4. Gravitational Waves

We now discuss properties of the GW signatures associated with our simulated systems as well as correlated EM+GW signatures. The gravitational waveforms from our simulations are almost identical to those of vacuum simulations, with point-wise differences of $< 10^{-2}\%$ for all the cases we considered. This is because the mass of the gas that is gravitationally bound to our binaries is many orders of magnitude smaller than the mass of the BBH.

As mentioned before, detection of correlated EM+GW oscillations from the same object would be a smoking gun for a BBH system on the way to coalescence and would directly link a detected GW source to its EM counterpart. The oscillations observed from the bremsstrahlung's relativistically beamed light are directly tied to the orbital dynamics of the binary and thus are also correlated with the frequency of the GWs. In order to compare the characteristic variability of the relativistically beamed bremsstrahlung light curve (Section 5.2) with that of the GWs, we overlay in Fig. 15 the light curves of the beamed bremsstrahlung emission and the magnitude of the gravitational waveforms for the two prograde-spinning BH cases (G1 and G2) during the inspiral phase. Vertical lines have been drawn to mark the peaks of the real part of the waveform. Clearly the frequency of oscillations in the light curve closely matches the GW frequency. No similar variability is visibly present in the bremsstrahlung light curve in run G3 since the asymmetry in spins inhibits the formation of the strong, symmetric density wakes. As most BBH systems in the universe are expected to be unequal-mass binaries, and thus have some inherent asymmetry, the likelihood of observing such correlated oscillations therefore depends on the extent to which asymmetries can modify the variability as well as the dominant mechanism that powers the emission.

Another form of EM variability associated with BH coalescences has been predicted to arise due to the effect of GW mass loss. If present, this variability is expected to be most prominent in geometrically thin circumbinary accretion disks in which transient shocks “light up” the gas disk in response to a changed gravitational potential of the central BH (Bode and Phinney 2007). It has been shown that transient shocks are absent in moderately thick, hotter disks, where $H/R \gtrsim f$ (f is the fractional mass loss due to emission of GW). In such flows the velocity of radial motions that arise in the gas due to perturbations in the gravitational potential is low with respect to the speed of sound and thus incapable of producing shocks (O’Neill et al. 2009). With fractional mass losses at the level of 3.6%, 5.0%, 6.3%, and 3.6% in runs G0-G3, respectively, we find no subsequent EM variability in our simulated systems due to this effect. This is consistent with the expectations based on studies described above since our gas cloud scenario also falls in the class of hot and geometrically thick accretion flows.

⁸ Note that we evaluate the Lorentz factor given the velocity of a parcel of fluid, while van Meter et al. (2009) evaluate the *collisional* Lorentz factor from relative velocities of converging particles.

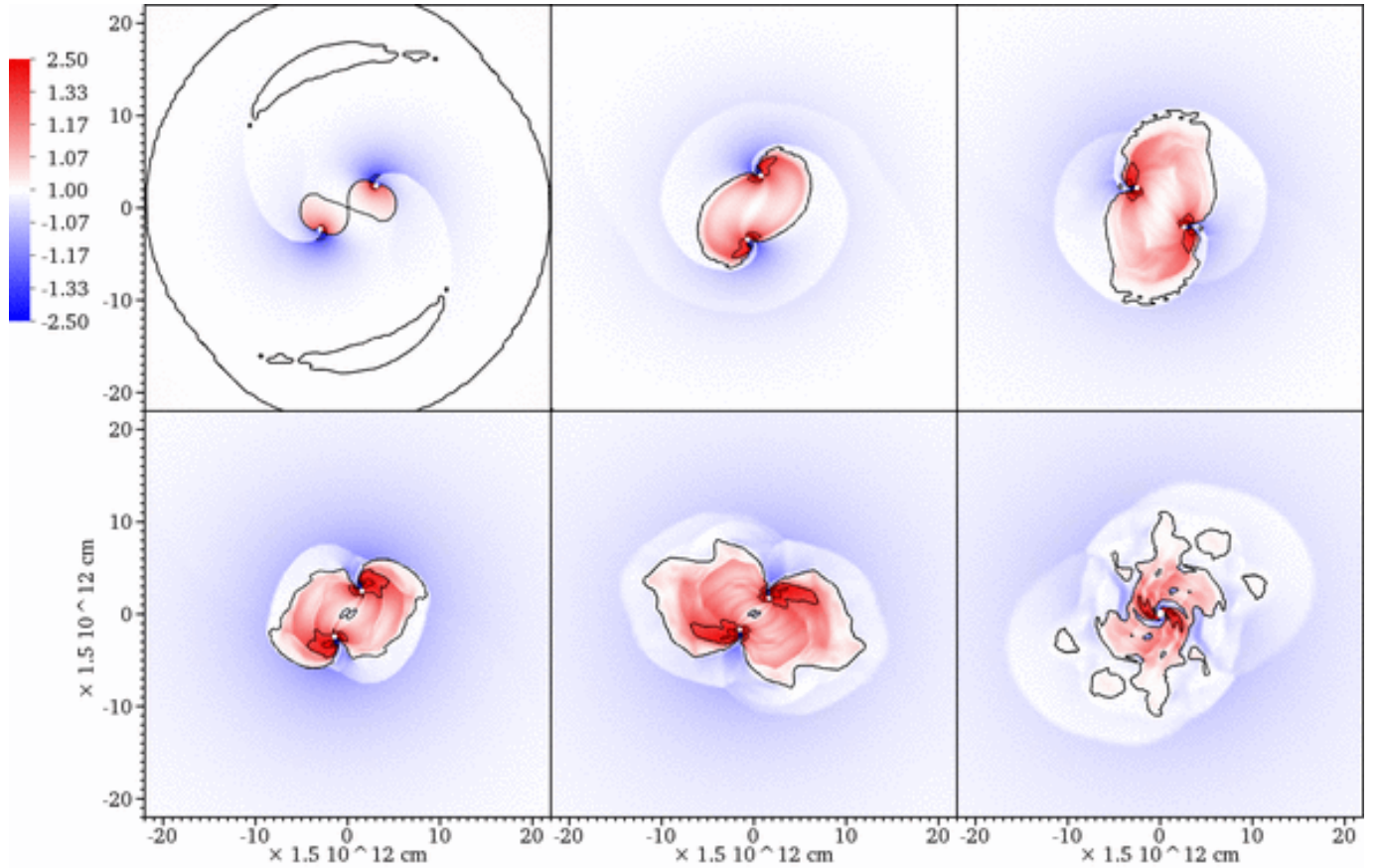


FIG. 13.— Snapshots of the Lorentz factor measured in the plane of the binary in run G2. Outgoing flows are shown in red and ingoing flows in blue (color online only), with the black contour line separating ingoing and outgoing flows. The gas between the BHs is flowing radially outwards. The snapshots shown are coincident with those depicted in Figures 2, 4, and 6.

Shocks and EM variability associated with the gas have also been predicted to arise from the GW recoil of the post-coalescence BH (Lippai et al. 2008; Shields and Bonning 2008; Megevand et al. 2009; Corrales et al. 2009; Rossi et al. 2009; Schnittman and Krolik 2008). From our four cases only the remnant BH in run G3 receives a “GW kick” as a consequence of an asymmetry in the emission of GWs. In this case, the up-down configuration of the spin vectors of the two BHs breaks the symmetry of the system and causes a fraction of linear momentum carried by GWs to be emitted preferentially in one direction. As a consequence of the conservation of linear momentum, the remnant BH recoils in the opposite direction with respect to the center of mass of the pre-coalescence binary with velocity of $\sim 180 \text{ km s}^{-1}$. No prompt shocks arise in run G3 due to the GW recoil, where the evolution follows the remnant BH to a total displacement of only $\sim 0.2M$ from the center of mass. The absence of shocks and EM signatures in our simulations is again not surprising given the properties of the gas and the short timescales covered by our simulations. The imprints of the recoil on the gas could, however, be noticeable on much longer timescales, in which case a recoiling BH can produce shocks or a trail of hot, X-ray emitting gas that extends out of the immediate center of a galaxy (Devecchi et al. 2009).

5.5. Observability of coalescences

In this section, we outline some observational strategies for the detection and monitoring of coalescing binaries based on the characteristic EM and GW signatures presented in this work.

Consider a binary of mass $10^7 M_{\odot}$ at a redshift of $z = 1$. With current expected LISA sensitivities, such a binary will be detectable by LISA during plunge and coalescence. Shortly before merger, the LISA error region could confine the location of such a binary to within a few tenths of a square degree on the sky (Lang and Hughes 2006). The exact size of the error region depends on a number of factors, including the location of the object on the sky, BH masses, and spin orientation. For instance, if the spin axes are misaligned, the orbital precession can further reduce the size of the error region to a few hundredths of a square degree.

The LISA error box hence marks a region on the sky relevant to EM searches for counterparts. Given our assumptions about the dominant emission mechanism in the vicinity of the BH binary it follows that $L_{\text{bol}} \sim L_{\text{brem}}$. The hot plasma cloud in our simulations is a natural source of high energy photons peaking in the γ -ray part of the spectrum at energies $kT_e \sim 1 \text{ MeV}$. Because of the higher sensitivity of the X-ray over γ -ray surveys in terms of observed flux, in the remainder of the discussion we focus on the observational strategy in the context of X-ray observations. The X-ray emission from our simulated sources would comprise a fraction of their bolometric luminosity and we estimate it by applying an empirical scaling in the form of a bolometric correction. Assuming a bolometric correction of $C_X = 15.8$, appropriate for low luminosity AGN (Ho 2009), we infer the X-ray luminosity associated with our binary, $L_X = L_{\text{bol}}/C_X \sim 10^{43} \text{ erg s}^{-1}$. A binary at $z = 1$ is at luminosity distance $d_L = 6.6 \text{ Gpc}$ (assuming a flat universe with matter parameter $\Omega_m = 0.27$ and Hubble parameter $h_0 = 0.71$). The observed X-ray flux from

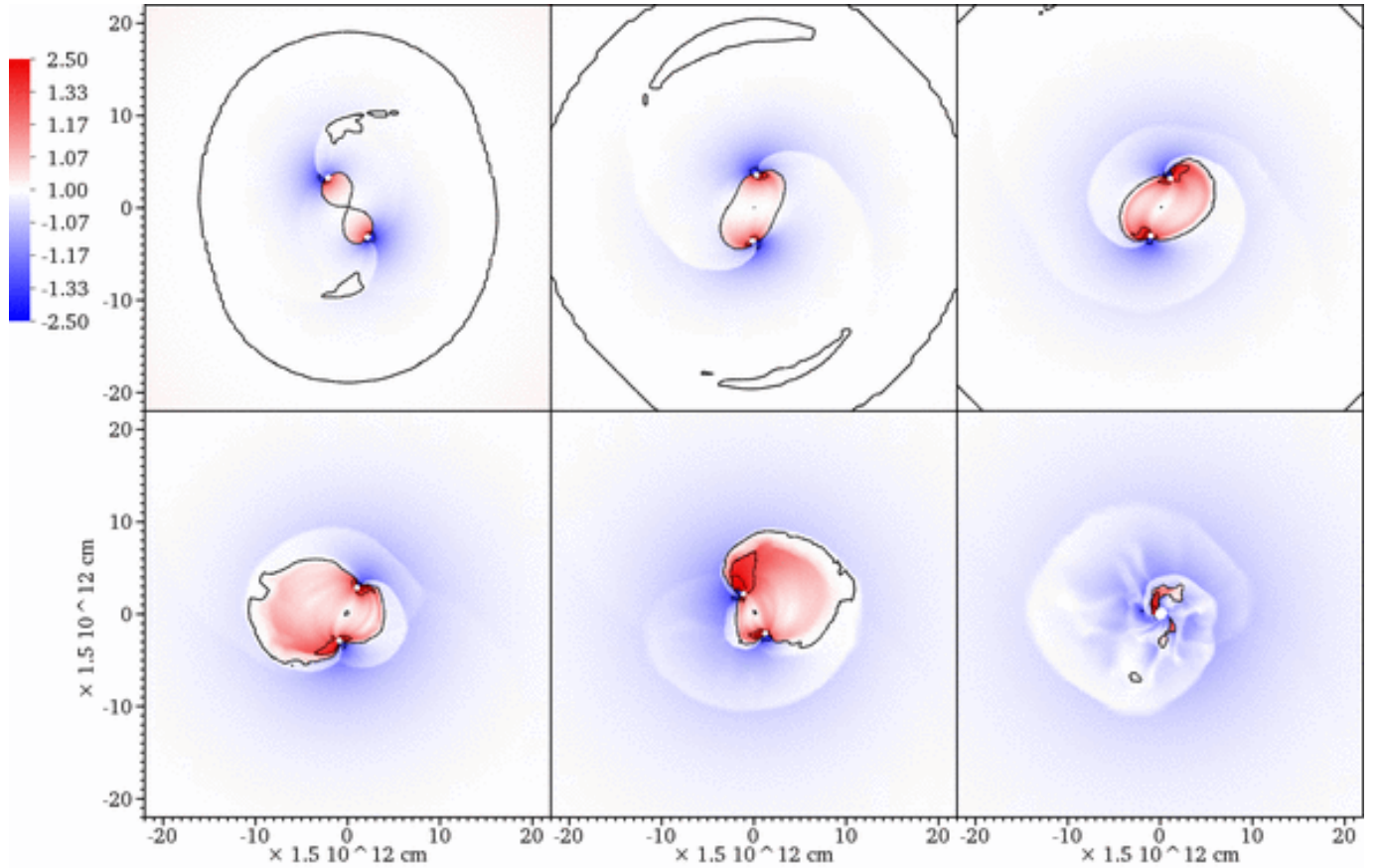


FIG. 14.— Same as in Fig. 13 but for the run G3. Snapshots shown are coincident with those in Figures 3, 5, and 7.

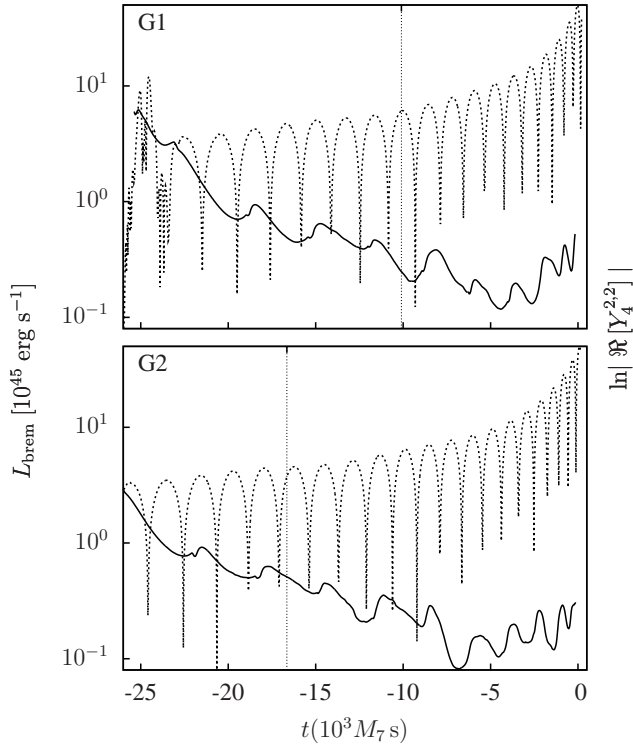


FIG. 15.— Comparison of bremsstrahlung and GW variability for the G1 (upper panel) and G2 (lower panel) runs. Real part of the waveform $\Re[\Psi_4^{2,2}]$ (dashed line) is superimposed on the top of the Doppler-boosted bremsstrahlung light curve (solid line). Vertical lines mark the maxima of the real part of the waveform.

this system is $F_X \sim 10^{-15} \text{ erg cm}^{-2} \text{ s}^{-1}$. According to our simulations, this level of luminosity will be observable for at least $t \gtrsim 400M = 2 \times 10^4 M_7 \text{ s}$ in the frame of the binary or, for a source at $z = 1$, for $t \gtrsim 4 \times 10^4 M_7 \text{ s}$ in the frame of the observer.

Of the future X-ray observatories that may operate contemporary with LISA, *IXO* and *EXIST* have planned sensitivities sufficient to observe high luminosity obscured AGN at $z \sim 0 - 2.5$ and low luminosity AGN at $z < 0.5$. Both X-ray instruments have a planned field of view (FOV) close to $20'$ in diameter and a flux sensitivity limit of $10^{-15} \text{ erg cm}^{-2} \text{ s}^{-1}$ achievable in $\sim 10^4 \text{ s}$ of exposure time. Given the above estimate for the X-ray flux, it follows that some of the brighter candidate AGN could be detected in as little as 1 hour of exposure. X-ray monitoring with ~ 1 -hour sampling frequency would allow a follow-up of the quasi-periodic variability close to the coalescence until the point where the orbital period of the binary becomes $\lesssim 1 \text{ hr}/(1+z)$. In order not to be masked by a natural variability intrinsic to most AGN, the magnitude of quasi-periodic oscillations should exceed few tens of percent of the luminosity of an AGN. Given a LISA error region smaller than $\sim 20'$, either X-ray instrument could cover it in a single exposure, hence allowing continuous monitoring of the X-ray luminosity curve.

Note that binaries with masses lower than $10^7 M_\odot$ will be detected by LISA during their inspiral phase as well as plunge and coalescence, thus including more orbital cycles prior to coalescence. This may facilitate some EM counterpart searches since they can be triggered earlier, but in some cases earlier detection will imply a trade-off in strength of GW signal. Because the GW signal is weaker during the inspiral

phase than during the plunge and coalescence, the LISA error region will be larger, and a day before the coalescence it may encompass a square degree range (Lang and Hughes 2006). In such a case, because the size of the LISA error region exceeds the planned FOV of any X-ray instrument, an observational strategy would require multiple exposure frames until the whole error region is tiled. In order to detect variability, the procedure would then need to be repeated and the error region scanned multiple times. Given a square degree error region and the 20' FOV of both future X-ray instruments, it would take about 9 exposures to cover the error region once, before a new snapshot of the field can be acquired. Because lower mass binaries are also expected to be less luminous ($L_X \sim 10^{40} \text{ erg s}^{-1}$ for $10^6 M_\odot$ binary), they would fall into a low luminosity AGN category and could only be monitored in the local universe out to a distance of $\sim 100 \text{ Mpc}$. A large initial error region and low luminosity make detection of the quasi-periodic variability a challenging prospect for lower mass systems. Nevertheless, a luminosity rise peaking at coalescence followed by a sudden drop-off can still be used as robust signatures for the EM detection of these binary systems. Following a detection, multi-wavelength coverage of the object on the sky would lead to localization of the source with an even higher precision, at the level of arcseconds and higher, and would allow a study of properties of the host galaxy.

While our discussion of observability of BH coalescences focuses on ‘‘LISA binaries’’ with masses of $10^7 M_\odot$ or less and the feasibility of coincident EM+GW detections, it is worth mentioning that a serendipitous EM detection of a BH coalescence may occur even before LISA, in the current era of observations. Such a detection would be most likely for more massive ($\sim 10^8 M_\odot$) and more luminous binary systems that could be ‘‘caught’’ by the current wide field of view observatories monitoring the high energy transient sky. Other forms of EM variability may also arise from mechanisms that were not captured by our simulations, such as radio, X-ray and γ -ray outbursts due to reconnection and effects of magnetic field lines close to the binary. Specifically, if a magnetic field with near-equipartition strength is present in the vicinity of a binary the synchrotron and inverse Compton radiation may dominate the emission in millimeter and high energy bands, respectively. Whether these phenomena can give rise to characteristic signatures that would uniquely point to a BBH coalescence event is a question of interest which remains to be studied in the context of MHD-NR calculations.

6. CONCLUSIONS

We presented the first fully general relativistic numerical hydrodynamics simulations of SMBH binaries in a gaseous environment through inspiral, plunge, and coalescence. The gaseous environment is a hot and turbulent gas cloud with physical properties reminiscent of accretion flows in low luminosity AGNs. The gas cloud was chosen as one of the characteristic scenarios representative of conditions in which pre-coalescence binaries may exist in galactic centers. Since the radial inflow speed in a hot gas cloud in our simulations is sufficiently high to prevent binary torques from evacuating most of the gas locally, accretion and interaction of the binaries with the gas continue uninterrupted throughout the merger. As a sample of the parameter space, we studied three symmetric, equal-mass BBH with spins of $a/M = 0, 0.4, 0.6$ aligned with the orbital angular momentum. In addition, we considered a fourth case of a binary with anti-aligned BH spins of magnitude $a/M = 0.4$ parallel to the orbital angular momentum. The

characteristic EM and GW signatures that arise from such interactions were the focus of this work. We summarize our most important results as follows:

- Our simulations show that correlated EM-GW variability can occur in merging binary systems immersed in hot gas flows. Specifically, we found EM variability arising due to the effects of relativistic beaming and Doppler boosting modulated by the binary orbital motion. In these systems the frequency of the EM oscillations is equal to that of the GWs and the maximum amplitude of variations in luminosity is a factor of ~ 2 .
- The variable EM emission in our simulations is powered by shocks triggered by the orbiting BHs. While quasi-periodic variability is present in all cases considered from inspiral through the plunge, it is not as pronounced in the case of a binary with asymmetric, prograde-retrograde spin configuration.
- In cases where quasi-periodic variability in luminosity may be weak or absent, additional signatures may be sought for in searches for EM counterparts. Our models indicate that, in cases where the luminosity is dominated by emission from the shocked gas, light curves may exhibit a gradual rise, arriving at a peak at the time of coalescence, followed by a sudden drop-off. If present, these two features are sufficiently robust to allow identification of an EM counterpart to a GW source.
- We estimate that most massive binaries detectable in the LISA band may be identified in EM searches out to $z \approx 1$. However, lower mass binaries and systems with gas densities lower than those considered here would fall into a class of low luminosity AGNs that could only be identified in the local universe.

In summary, if coincident variability can be observed in both light and GWs from the same object, this signature would be convincing evidence for an impending BBH coalescence. Our results suggest some encouraging prospects for such detections. Nevertheless, given the extent of the parameter space involved in coalescing BBHs interacting with gas, more follow-up work is needed. In particular, since most of the SMBH binaries in the universe are expected to involve unequal masses and general spin orientations, it is important to further explore the parameter space to investigate how common situations with characteristic EM signatures such as those in the present work may be. Furthermore, because the thermodynamic properties of the surrounding gas can significantly influence the properties of EM signals, in the future we will also consider other scenarios for gaseous environments around SMBHs in galactic centers, such as a rotating gas cloud and circumbinary accretion disk.

We thank Mike Eracleous, Cole Miller, and Sean O’Neill for useful comments and suggestions and James Healy for computational infrastructure. T. Bogdanović is grateful to Richard Mushotzky, Scott Noble, and Tom Maccarone for stimulating discussions. This work was supported in part by the NSF grants 0653443, 0855892, 0914553, 0941417, 0903973. Support for Bogdanović provided by NASA through Einstein Postdoctoral Fellowship Award PF9-00061

issued by the Chandra X-ray Observatory Center, which is operated by the Smithsonian Astrophysical Observatory for and on behalf of the NASA under contract NAS8-03060. Computations described in this paper were carried out under Teragrid allocation TG-MCA08X009.

tations described in this paper were carried out under Teragrid allocation TG-MCA08X009.

REFERENCES

- M. G. Haehnelt and G. Kauffmann, *MNRAS* **336**, L61 (2002), arXiv:astro-ph/0208215.
- M. Volonteri, F. Haardt, and P. Madau, *ApJ* **582**, 559 (2003a), arXiv:astro-ph/0207276.
- J. Kormendy and D. Richstone, *ARA&A* **33**, 581 (1995).
- D. Richstone, E. A. Ajhar, R. Bender, G. Bower, A. Dressler, S. M. Faber, A. V. Filippenko, K. Gebhardt, R. Green, L. C. Ho, et al., *Nature* **395**, A14+ (1998), arXiv:astro-ph/9810378.
- B. M. Peterson and A. Wandel, *ApJ* **540**, L13 (2000), arXiv:astro-ph/0007147.
- L. Ferrarese and H. Ford, *Space Science Reviews* **116**, 523 (2005), arXiv:astro-ph/0411247.
- M. Volonteri, P. Madau, and F. Haardt, *Astrophys. J.* **593**, 661 (2003b), arXiv:astro-ph/0304389.
- M. Volonteri, F. Haardt, P. Madau, and A. Sesana, in *Astrophysics and Space Science*, edited by M. Plionis (2004), vol. 301 of *Astrophysics and Space Science Library*, p. 227.
- M. Micic, K. Holley-Bockelmann, S. Sigurdsson, and T. Abel, *Mon. Not. R. Astron. Soc.* **380**, 1533 (2007), arXiv:astro-ph/0703540.
- A. Sesana, M. Volonteri, and F. Haardt, *MNRAS* **377**, 1711 (2007), arXiv:astro-ph/0701556.
- B. Kocsis, Z. Frei, Z. Haiman, and K. Menou, *ApJ* **637**, 27 (2006), arXiv:astro-ph/0505394.
- S. A. Hughes and D. E. Holz, *Classical and Quantum Gravity* **20**, 65 (2003), arXiv:astro-ph/0212218.
- T. Bogdanović, M. Eracleous, and S. Sigurdsson, *New Astron. Rev.* **53**, 113 (2009), 0909.0516.
- S. Kazantzidis, L. Mayer, M. Colpi, P. Madau, V. P. Debattista, J. Wadsley, J. Stadel, T. Quinn, and B. Moore, *ApJ* **623**, L67 (2005), arXiv:astro-ph/0407407.
- P. J. Armitage and P. Natarajan, *ApJ* **567**, L9 (2002), arXiv:astro-ph/0201318.
- A. Escala, R. B. Larson, P. S. Coppi, and D. Mardones, *ApJ* **607**, 765 (2004), arXiv:astro-ph/0310851.
- A. Escala, R. B. Larson, P. S. Coppi, and D. Mardones, *ApJ* **630**, 152 (2005), arXiv:astro-ph/0406304.
- M. Dotti, M. Colpi, F. Haardt, and L. Mayer, *MNRAS* **379**, 956 (2007), arXiv:astro-ph/0612505.
- L. Mayer, S. Kazantzidis, P. Madau, M. Colpi, T. Quinn, and J. Wadsley, *Science* **316**, 1874 (2007), 0706.1562.
- M. Colpi, M. Dotti, L. Mayer, and S. Kazantzidis, *ArXiv e-prints* (2007), 0710.5207.
- A. I. MacFadyen and M. Milosavljević, *ApJ* **672**, 83 (2008), arXiv:astro-ph/0607467.
- K. Hayasaki, S. Mineshige, and L. C. Ho, *ApJ* **682**, 1134 (2008), 0708.2555.
- J. Cuadra, P. J. Armitage, R. D. Alexander, and M. C. Begelman, *MNRAS* **393**, 1423 (2009), 0809.0311.
- M. Milosavljević and E. S. Phinney, *ApJ* **622**, L93 (2005), arXiv:astro-ph/0410343.
- E. J. L. Quataert, Ph.D. thesis, AA(HARVARD UNIVERSITY) (1999).
- A. Ptak, Y. Terashima, L. C. Ho, and E. Quataert, *ApJ* **606**, 173 (2004), arXiv:astro-ph/0401524.
- R. S. Nemmen, T. Storchi-Bergmann, F. Yuan, M. Eracleous, Y. Terashima, and A. S. Wilson, *ApJ* **643**, 652 (2006), arXiv:astro-ph/0512540.
- M. Elitzur and L. C. Ho, *ApJ* **701**, L91 (2009), 0907.3752.
- T. Bogdanović, C. S. Reynolds, and M. C. Miller, *ApJ* **661**, L147 (2007), arXiv:astro-ph/0703054.
- F. Herrmann, I. Hinder, D. M. Shoemaker, P. Laguna, and R. A. Matzner, *Phys. Rev. D* **76**, 084032 (2007a), arXiv:0706.2541.
- M. Koppitz, D. Pollney, C. Reisswig, L. Rezzolla, J. Thornburg, P. Diener, and E. Schnetter, *Physical Review Letters* **99**, 041102 (2007), arXiv:gr-qc/0701163.
- M. Campanelli, C. Lousto, Y. Zlochower, and D. Merritt, *Astrophys. J. Lett.* **659**, L5 (2007a), arXiv:gr-qc/0701164.
- M. Campanelli, C. O. Lousto, Y. Zlochower, and D. Merritt, *Physical Review Letters* **98**, 231102 (2007b), arXiv:gr-qc/0702133.
- J. A. González, M. Hannam, U. Sperhake, B. Brügmann, and S. Husa, *Physical Review Letters* **98**, 231101 (2007), arXiv:gr-qc/0702052.
- J. G. Baker, W. D. Boggs, J. Centrella, B. J. Kelly, S. T. McWilliams, M. C. Miller, and J. R. van Meter, *Astrophys. J.* **668**, 1140 (2007), arXiv:astro-ph/0702390.
- J. D. Schnittman and A. Buonanno, *Astrophys. J. Lett.* **662**, L63 (2007), arXiv:astro-ph/0702641.
- J. R. van Meter, J. H. Wise, M. C. Miller, C. S. Reynolds, J. M. Centrella, J. G. Baker, W. D. Boggs, B. J. Kelly, and S. T. McWilliams, *ArXiv e-prints* (2009), 0908.0023.
- C. Palenzuela, M. Anderson, L. Lehner, S. L. Liebling, and D. Neilsen, *Physical Review Letters* **103**, 081101 (2009a), 0905.1121.
- C. Palenzuela, L. Lehner, and S. Yoshida, *ArXiv e-prints* (2009b), 0911.3889.
- M. C. Washik, J. Healy, F. Herrmann, I. Hinder, D. M. Shoemaker, P. Laguna, and R. A. Matzner, *Physical Review Letters* **101**, 061102 (2008), arXiv:0802.2520.
- I. Hinder, B. Vaishnav, F. Herrmann, D. M. Shoemaker, and P. Laguna, *Phys. Rev. D* **77**, 081502 (2008), arXiv:0710.5167.
- F. Herrmann, I. Hinder, D. Shoemaker, P. Laguna, and R. A. Matzner, *Astrophys. J.* **661**, 430 (2007b), arXiv:gr-qc/0701143.
- F. Herrmann, I. Hinder, D. Shoemaker, and P. Laguna, *Classical and Quantum Gravity* **24**, 33 (2007c), arXiv:gr-qc/0601026.
- T. Bode, D. Shoemaker, F. Herrmann, and I. Hinder, *Phys. Rev. D* **77**, 044027 (2008), arXiv:0711.0669.
- T. Bode et al., *Phys. Rev. D* **80**, 024008 (2009), 0902.1127.
- M. Campanelli, C. O. Lousto, P. Marronetti, and Y. Zlochower, *Physical Review Letters* **96**, 111101 (2006a), arXiv:gr-qc/0511048.
- J. G. Baker, J. Centrella, D.-I. Choi, M. Koppitz, and J. van Meter, *Physical Review Letters* **96**, 111102 (2006), arXiv:gr-qc/0511103.
- S. Husa, I. Hinder, and C. Lechner, *Computer Physics Communications* **174**, 983 (2006), gr-qc/0404023.
- G. Allen, T. Goodale, and E. Seidel, in *7th Symposium on the Frontiers of Massively Parallel Computation-Frontiers 99* (IEEE, New York, 1999).
- E. Schnetter, S. H. Hawley, and I. Hawke, *Class. Quant. Grav.* **21**, 1465 (2004).
- Whisky-web, Whisky, EU Network GR Hydrodynamics Code: <http://www.whiskycode.org>.
- L. Baiotti, I. Hawke, P. Montero, and L. Rezzolla, in *Computational Astrophysics in Italy: Methods and Tools*, edited by R. Capuzzo-Dolcetta (Mem. Soc. Astron. It. Suppl., Trieste, 2003), vol. 1, p. 327.
- J. M. Martí, J. M. Ibáñez, and J. M. Miralles, *Phys. Rev. D* **43**, 3794 (1991).
- F. Banyuls, J. A. Font, J. M. Ibáñez, J. M. Martí, and J. A. Miralles, *Astrophys. J.* **476**, 221 (1997).
- J. Ibáñez, M. Aloy, J. Font, J. Martí, J. Miralles, and J. Pons, in *Godunov methods: theory and applications*, edited by E. Toro (Kluwer Academic/Plenum Publishers, New York, 2001).
- J. A. Faber, T. W. Baumgarte, Z. B. Etienne, S. L. Shapiro, and K. Taniguchi, *Phys. Rev. D* **76**, 104021 (2007), arXiv:0708.2436.
- M. Ansorg, B. Brügmann, and W. Tichy, *Phys. Rev. D* **70**, 064011 (2004).
- J. M. Bowen and J. W. York, Jr., *Phys. Rev. D* **21**, 2047 (1980).
- J. W. York, in *Sources of Gravitational Radiation*, edited by L. L. Smarr (Cambridge University Press, Cambridge, UK, 1979), pp. 83–126, ISBN 0-521-22778-X.
- R. C. Tolman, *Phys. Rev.* **55**, 364 (1939).
- J. R. Oppenheimer and G. Volkoff, *Phys. Rev.* **55**, 374 (1939).
- C. W. Misner, K. S. Thorne, and J. A. Wheeler, *Gravitation* (W. H. Freeman, San Francisco, 1973).
- K. Hayasaki, S. Mineshige, and H. Sudou, *PASJ* **59**, 427 (2007), arXiv:astro-ph/0609144.
- A. Buonanno, Y. Chen, and T. Damour, *Physical Review D (Particles, Fields, Gravitation, and Cosmology)* **74**, 104005 (pages 26) (2006), 0508067, URL <http://link.aps.org/abstract/PRD/v74/e104005>.
- L. E. Kidder, *Phys. Rev. D* **52**, 821 (1995).
- M. Campanelli, C. O. Lousto, and Y. Zlochower, *Phys. Rev. D* **74**, 041501 (2006b), arXiv:gr-qc/0604012.
- S. Ichimaru, *ApJ* **214**, 840 (1977).
- M. J. Rees, M. C. Begelman, R. D. Blandford, and E. S. Phinney, *Nature* **295**, 17 (1982).
- R. Narayan and I. Yi, *ApJ* **428**, L13 (1994), arXiv:astro-ph/9403052.
- G. B. Rybicki and A. P. Lightman, *Radiative Processes in Astrophysics* (1986).
- E. Quataert, *Astronomische Nachrichten Supplement* **324**, 435 (2003), arXiv:astro-ph/0304099.
- B. D. Farris, Y. T. Liu, and S. L. Shapiro (2009), 0912.2096.
- P. Natarajan and J. E. Pringle, *ApJ* **506**, L97 (1998), arXiv:astro-ph/9808187.
- P. Natarajan and P. J. Armitage, *MNRAS* **309**, 961 (1999), arXiv:astro-ph/9812001.
- A. R. King, S. H. Lubow, G. I. Ogilvie, and J. E. Pringle, *MNRAS* **363**, 49 (2005), arXiv:astro-ph/0507098.

- G. Lodato and J. E. Pringle, *MNRAS* **368**, 1196 (2006), arXiv:astro-ph/0602306.
- G. Lodato and J. E. Pringle, *MNRAS* **381**, 1287 (2007), 0708.1124.
- P. C. Fragile, O. M. Blaes, P. Anninos, and J. D. Salmonson, *ApJ* **668**, 417 (2007), 0706.4303.
- A. Perego, M. Dotti, M. Colpi, and M. Volonteri, ArXiv e-prints (2009), 0907.3742.
- M. Dotti, M. Volonteri, A. Perego, M. Colpi, M. Ruzkowsky, and F. Haardt, ArXiv e-prints (2009), 0910.5729.
- N. Bode and S. Phinney, *APS Meeting Abstracts* pp. 1010+ (2007).
- S. M. O'Neill, M. C. Miller, T. Bogdanović, C. S. Reynolds, and J. D. Schnittman, *ApJ* **700**, 859 (2009), 0812.4874.
- Z. Lippai, Z. Frei, and Z. Haiman, *Ap. J. Lett.* **676**, L5 (2008), arXiv:0801.0739.
- G. A. Shields and E. W. Bonning, *Astrophys. J.* **682**, 758 (2008), arXiv:0802.3873.
- M. Megevand et al., *Phys. Rev.* **D80**, 024012 (2009), 0905.3390.
- L. R. Corrales, Z. Haiman, and A. MacFadyen (2009), 0910.0014.
- E. M. Rossi, G. Lodato, P. J. Armitage, J. E. Pringle, and A. R. King, *MNRAS* pp. 1726+ (2009), 0910.0002.
- J. D. Schnittman and J. H. Krolik, *ApJ* **684**, 835 (2008), 0802.3556.
- B. Devecchi, E. Rasia, M. Dotti, M. Volonteri, and M. Colpi, *MNRAS* **394**, 633 (2009), 0805.2609.
- R. N. Lang and S. A. Hughes, *Phys. Rev. D* **74**, 122001 (2006), arXiv:gr-qc/0608062.
- L. C. Ho, *ApJ* **699**, 626 (2009), 0906.4104.